Orbital angular momentum mode analysis with a micro mirror array

P. F. Chimento

January 28, 2008

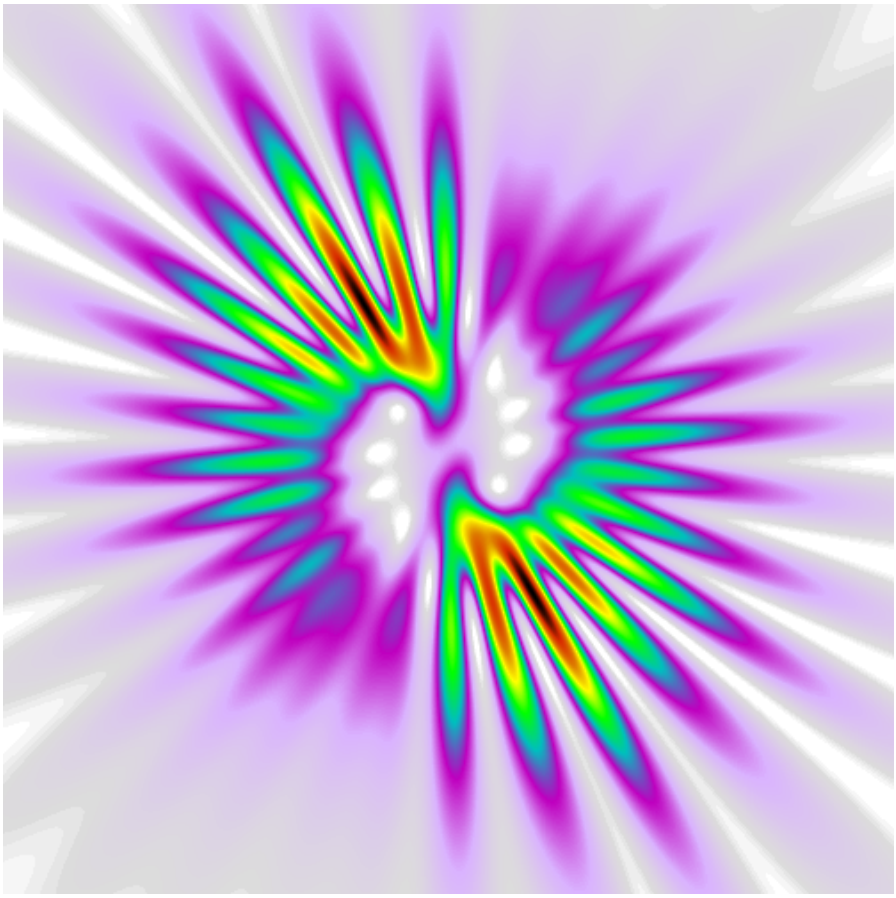

The cover illustration shows the far field intensity distribution of a Gaussian beam that has encountered a 19-segment phase plate with an effective dimensionality of 65. This phase plate was made out of confectionery and put atop a cake in honor of Professor Han Woerdman's birthday, and thus was a "pie phase plate" in the most literal sense.

Contents

1

Introduction

Two photons can be put in a state in which their collective wave function cannot be expressed as the product of two individual wave functions. One example, in the orthonormal basis $|H\rangle, |V\rangle$ of horizontal and vertical linear polarization, is

$$\Psi_{12} = a\,|H\rangle_1\,|V\rangle_2 + b\,|V\rangle_1\,|H\rangle_2\,, \tag{1.1}$$

where $|a|^2 + |b|^2 = 1$. Such states are called entangled and have been responsible for much interesting theoretical and experimental research throughout the 20th century, including the entire field of quantum information processing. The signal and idler photons of a down-conversion process form an entangled pair, as long as they cannot be distinguished in any way.

Polarization entanglement of photons is called two-dimensional, because the states of the individual photons can be fully described in the two-dimensional linear polarization state space.

Photons also carry orbital angular momentum (OAM), or more accurately, can exist in a mode that carries OAM. This mode is a linear combination of states with a quantized OAM of $l\hbar$, where $l = 0, \pm1, \pm2, \ldots, \pm\infty$. There is thus an infinite number of OAM eigenstates, compared to only two polarization states. The orbital angular momentum of a photon expresses itself physically in the azimuthal phase profile of the associated mode [3].

In 2001, Mair et al. [10] demonstrated the first multidimensionally entangled photon states, using the three lowest-order OAM modes $l = -1, 0, 1$. In general, OAM entangled states can be written as an inseparable two-photon wave function of the form

$$\Psi_{12} = \sum_l a_l \left|l\right\rangle_1 \left|-l\right\rangle_2, \tag{1.2}$$

where $\sum |a_l|^2 = 1$ and $|l\rangle$ denotes the eigenstate with orbital angular momentum $l\hbar$. This entangled wave function can be projected onto the *infinite-dimensional* space spanned by the OAM eigenstates, and is therefore called multidimensional. Orbital angular momentum is conserved in down-conversion, so the signal and idler photons of a down-conversion process can also be used to generate pairs of photons in an entangled OAM state.

Recent work has concerned analyzers for measuring the projection of OAM entangled states onto pure OAM states. At the heart of such an analyzer is a phase plate[1], a transmission or reflection element that performs a certain azimuthal phase operation on an incident electromagnetic field. The phase plate changes the OAM state into a different input state, which is a linear combination of OAM eigenstates. The projection of the resulting input state onto the $|0\rangle$ state is then measured using a single-mode fiber. The latter only supports modes with zero OAM, which correspond to Gaussian modes.

The desired projection can be selected by choosing an appropriate phase plate. Any phase plate has a set of coupling coefficients P_l which represent the probability of a photon's orbital angular momentum increasing by $l\hbar$. Alternatively, when a Gaussian passes through a phase plate and is transformed into a linear combination of OAM eigenstates, P_l is the square of the magnitude of the $|l\rangle$ component.

Although the OAM space is infinite-dimensional, no analyzer can address all dimensions at once. In [13] a measure called the effective dimensionality is introduced which represents the number of dimensions of the space that an analyzer can effectively address. It is equal to:

$$D_{\text{eff}} = \frac{1}{\sum_{l=-\infty}^{\infty} P_l^2}. \tag{1.3}$$

If the distribution of the coupling coefficients is narrow, with a high peak, then $\sum P_l^2$ will be close to 1. If the distribution is wide, it will become smaller, yielding a higher effective dimensionality. Applying this measure to the case of polarization eigenstates, we have $P_H = \frac{1}{2}$, $P_V = \frac{1}{2}$, and thus $D_{\text{eff}} = 2$.

[1] The phase plate does not have to be an actual plate; as in several of the experiments described in [12], it could also be a phase hologram. However, in light of recent work, we will speak of a phase plate here.

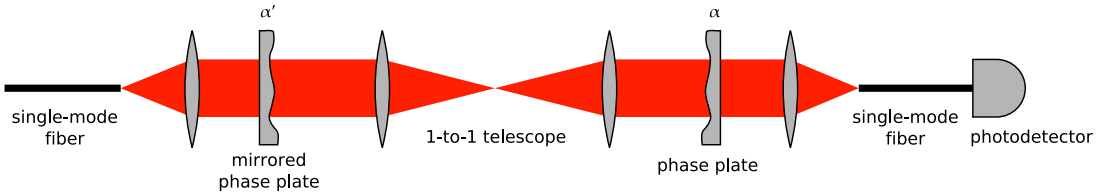

Figure 1.1: Sketch of an experiment for measuring the effective dimensionality of an analyzer [13].

The effective dimensionality of an analyzer can be measured experimentally. Figure 1.1 shows the experimental setup that is used to determine D_{eff}. Monochromatic light in a fundamental Gaussian (zero OAM) mode passes through a phase plate oriented at angle α' (effectively a mirrored analyzer) and is then coupled into an analyzer with the same phase plate oriented at angle α. The intensity is measured as α is rotated full circle, and the effective dimensionality is equal to 2π times the inverse of the area under the intensity curve as a function of $\alpha - \alpha'$ [13].

In previous experiments, the phase plate has always been a physical structure carrying an immutable phase operation. Recently, programmable devices have been developed which allow an arbitrary phase profile to be imprinted onto a field. This research concerns the characterization of one such device, a micro mirror array (MMA) made available by the Fraunhofer Institute for Photonic Microsystems under the name *MEMS Phase Former Kit*. It consists of a 240×200 array of 40×40 μm mirrors, which can retract individually up to a distance of about 350 nm. This makes it possible to control the phase of an incident light beam in the visible range by assigning a phase difference between zero and 2π radians to each pixel individually.

Furthermore, the suitability of this MMA as a dynamic replacement for the static phase plate in an analyzer will be investigated. The author builds upon Johan de Jong's results [4, ch. 4], by examining the influence of polarization, anti-aliasing, and how diffraction from the mirrors' mechanical structure causes effects not found in static phase plates.

2

Phase plates and orbital angular momentum mode expansion

Several types of phase plates are relevant to this research, either because there is an interest in using them in entanglement experiments or because they are suitable for use in characterizing the MMA. A brief analytical description of each of these will be visited, in order to lay a mathematical foundation for the far-field experiments conducted later on.

A phase plate can be a transmission or reflection element, performing a phase operation by means of a variation in thickness or index of refraction in the former case, or a variation in surface height in the latter. We will consider reflective phase plates in this chapter, but without loss of generality. In addition, only angular phase plates, i.e., plates in which the imprinted phase function is purely a function of the azimuthal coordinate θ, will be examined.

A phase plate can be usefully characterized by studying the far-field intensity distribution of the light that emerges when a Gaussian beam is incident on it. Each phase plate can be described by an azimuthal transfer function $H(\theta)$ and thus the far-field intensity distribution of a given input field $E_{\text{in}}(r,\theta)$ is given by[1]:

$$I_{\text{FF}}(R,\Theta) \propto |\mathcal{F}\{H(\theta)E_{\text{in}}(r,\theta)\}|^2. \tag{2.1}$$

[1]Note that the capital letter pairs X,Y and R,Θ indicate the Fourier-transformed (far-field) Cartesian and polar coordinates respectively, and the lowercase pairs x,y and r,θ indicate the near field.

Unless stated otherwise, we will consider a Gaussian input field with a flat phase front, $1/e$ radius w, and complex amplitude E_0:

$$E_{\text{in}}(r) \propto E_0 e^{-r^2/w^2}. \tag{2.2}$$

Since the phase plates under consideration only perform azimuthally dependent phase operations, the output field $H(\theta)E(r)$ is separable.

The azimuthal component of any electromagnetic field can be written as a linear combination of orbital angular momentum (OAM) modes. This is important in entanglement experiments, where we wish to use the phase plates as mode converters. We can decompose the output field of each phase plate into OAM eigenstates by writing the near field, expressed in polar coordinates, as a complex Fourier series in $e^{-il\theta}$,

$$E(r,\theta) = \sum_{l=-\infty}^{\infty} c_l E_{\text{in}}(r) e^{-il\theta}, \tag{2.3}$$

where:

$$c_l = \frac{1}{2\pi} \int_0^{2\pi} H(\theta) e^{il\theta} d\theta. \tag{2.4}$$

Since the near field is separable, c_l is effectively the complex Fourier series of $H(\theta)$, and the Fourier term $e^{-il\theta}$ coincides with the orbital angular momentum eigenmodes. The coupling coefficient P_l, or the probability for each photon with orbital angular momentum 0 to be converted to l, is equal to:

$$P_l = |c_l|^2. \tag{2.5}$$

The effective dimensionality can then be calculated using (1.3).

2.1 Constant phase plate

The constant phase plate is a trivial case, used to examine the far-field effects of the MMA's diffracting structure in section 4.2. It is simply a flat surface which imparts a constant phase delay on the entire beam and thus is indistinguishable from no phase difference at all. Its transfer function is $H = 1$; it does not change the OAM, thus $P_l = \delta_{l0}$, where δ is the Kronecker delta; and the far field is identical to the case of no phase plate:

$$I_{\text{FF}}(R) \propto \pi^2 w^4 |E_0|^2 e^{-2\pi^2 w^2 R^2}. \tag{2.6}$$

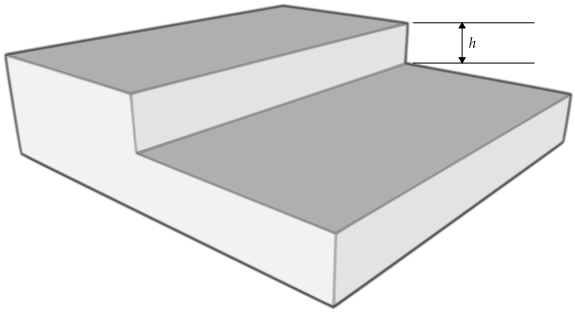

Figure 2.1: A Heaviside phase plate. The plate has a height dislocation h along one axis which causes a phase dislocation proportional to h/λ along one axis of an impinging electric field.

2.2 Heaviside phase plate

The Heaviside phase plate is named for the Heaviside step function, which its cross-section resembles. It is a flat plate with half of it raised by a height h, creating a dislocation in the center (see figure 2.1). In this case it is more convenient to consider the problem in Cartesian coordinates. The Heaviside phase plate adds a phase of $\phi \propto h/\lambda$ to one half of the beam:

$$H(x) = \begin{cases} 1, & x < 0 \\ e^{-i\phi}, & x \geq 0. \end{cases} \tag{2.7}$$

The far-field intensity of a Gaussian beam after a Heaviside phase plate is given by

$$I_{\mathrm{FF}}(X,Y) \propto 2\pi w^4 |E_0|^2 e^{-2\pi^2 w^2 Y^2} \left(\frac{\pi}{4}(1+\cos\phi) e^{-2\pi^2 w^2 X^2} \right. \\ \left. - \sqrt{\pi}\sin\phi\, e^{-\pi^2 w^2 X^2} D(\pi w X) + (1-\cos\phi)(D(\pi w X))^2 \right), \tag{2.8}$$

where $D(x)$ is the Dawson integral (A.6). This expression is derived in appendix A.1.

For the special case that $\phi = 0$ (i.e. a constant phase plate), (2.8) reduces to the far field of the original Gaussian, eq. (2.6). When $\phi = \pi/2$, (2.8) can be factored as:

$$I_{\mathrm{FF}}(X,0) \propto 2\pi w^4 |E_0|^2 \left(\sqrt{\frac{\pi}{4}} e^{-\pi^2 w^2 X^2} - D(\pi w X) \right)^2. \tag{2.9}$$

When $\phi = \pi$, the far field consists of two equal peaks:

$$I_{\mathrm{FF}}(X,0) \propto 4\pi w^4 |E_0|^2 (D(\pi w X))^2. \tag{2.10}$$

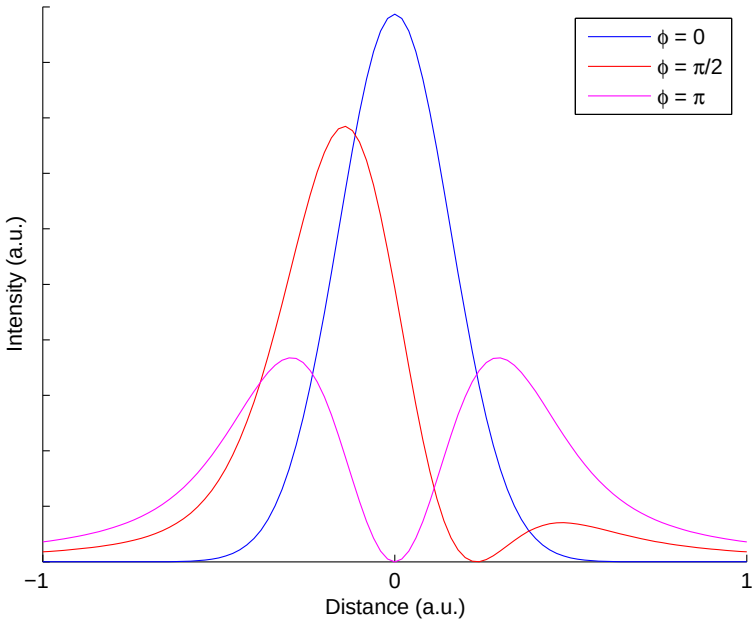

Figure 2.2: Cross-section of the far-field intensity distribution of a Gaussian beam that has encountered a Heaviside phase plate, for various values of the phase dislocation ϕ.

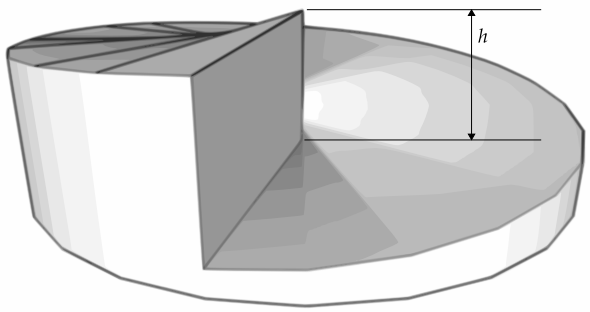

Figure 2.3: A spiral phase plate of height h. The plate has a helical ramp in which the height increases linearly from 0 to h.

These three cases are illustrated in figure 2.2.

As an OAM mode analyzer, an HPP with a phase step of $\phi = \pi$ has, according to (2.5), coupling coefficients of

$$P_l = \begin{cases} 0, & l \text{ even} \\ \dfrac{4}{\pi^2 l^2}, & l \text{ odd}, \end{cases} \tag{2.11}$$

which sum to an effective dimensionality of 3, by (1.3).

2.3 Spiral phase plate

The spiral phase plate imparts a helical phase onto a beam. It is shaped like a screw, with a dislocation of a certain height h (see figure 2.3). We define the vorticity Q [12, p. 22] of a spiral phase plate as h/λ.

For large Q and large λ, a spiral phase plate with the appropriate surface height may become impracticable since h must then become very large. However, the same effect on the field's phase can be produced by taking the phase modulo 2π, the phase analogue of a Fresnel lens' discontinuous curvature:

$$H(\theta) = e^{-i(Q\theta \bmod 2\pi)} = e^{-iQ\theta}. \tag{2.12}$$

An expression for the far field intensity distribution of a Gaussian beam after passing a spiral phase plate with integer Q is derived in appendix A.2:

$$I_{\mathrm{FF}}(R) \propto \tfrac{1}{4}|E_0|^2\pi^5 w^6 R^2 e^{-\pi^2 w^2 R^2} \left(I_{(|Q|-1)/2}(\tfrac{1}{2}\pi^2 w^2 R^2) - I_{(|Q|+1)/2}(\tfrac{1}{2}\pi^2 w^2 R^2) \right)^2, \tag{2.13}$$

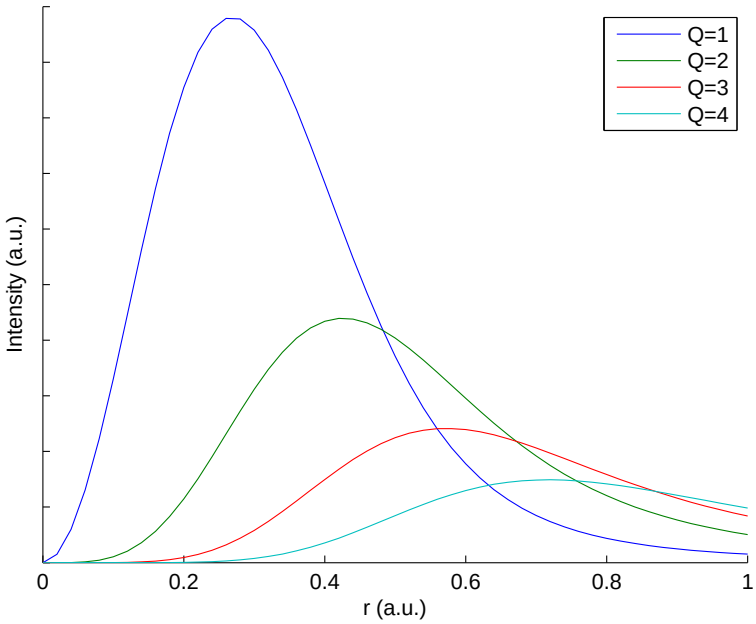

Figure 2.4: Radial section (constant θ) of the far-field intensity distribution of a Gaussian beam after encountering a spiral phase plate of integer vorticity Q.

where $I_\alpha(z)$ denotes the modified Bessel function of the first kind. A radial section of this intensity distribution is illustrated in figure 2.4 for different integer values of Q.

An SPP with fractional Q produces a more complicated far-field pattern and an analytical expression is not derived here. However, the decomposition of the near field of an SPP into OAM modes by eq. (2.5) is simpler. For $Q \in \mathbb{Z}$, we have the trivial expression $P_l = \delta_{lQ}$, where δ is the Kronecker delta. For SPPs of half-integer vorticity, we have, by eqs. (2.4) and (2.5),

$$P_l = \frac{1}{\pi^2 (l - Q)^2}, \tag{2.14}$$

and, by (1.3), an effective dimensionality of 3.

The spiral phase plates used in previous experiments were manufactured at Philips using a process described in [12, pp. 46–47]. The phase plates are not currently used in any research by Philips, but are convenient to manufacture there, since the same process is also used to manufacture certain lenses, and because of the contacts between Philips and the Quantum Optics and Quantum Information group.

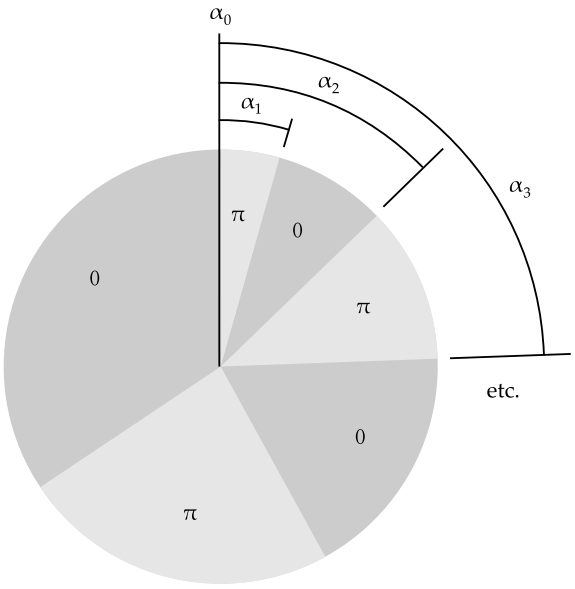

Figure 2.5: Pie slice angles α_n of a pie phase plate.

2.4 Pie phase plate

The pie phase plate is composed of N 'pie slices' with phase π. For any N, there is a certain combination of pie slice angles α_n, where $0 \leq n \leq 2N-1$, which maximizes the effective dimensionality D_{eff}. For the mathematics to come, it is useful to define $\alpha_0 = 0$. The angles α_n are illustrated in figure 2.5.

The transfer function of a pie phase plate is:

$$H(\theta) = \begin{cases} (-1)^n, & \alpha_{n-1} \leq \theta < \alpha_n, \quad 1 \leq n < 2N-1 \\ 1, & \alpha_{2N-1} \leq \theta < 2\pi. \end{cases} \tag{2.15}$$

An expression for the far-field intensity distribution of a Gaussian after a pie phase plate with an arbitrary number of slices N and arbitrary angles α_n is derived in appendix A.3. Its coupling coefficients P_l are given by

$$P_l = \begin{cases} \left(1 + \dfrac{1}{\pi} \displaystyle\sum_{p=1}^{2N-1} (-1)^p \alpha_p\right)^2, & l = 0 \\ \dfrac{1}{\pi^2 l^2} \left| \displaystyle\sum_{p=0}^{2N-1} (-1)^p e^{il\alpha_p} \right|^2, & l \neq 0, \end{cases} \tag{2.16}$$

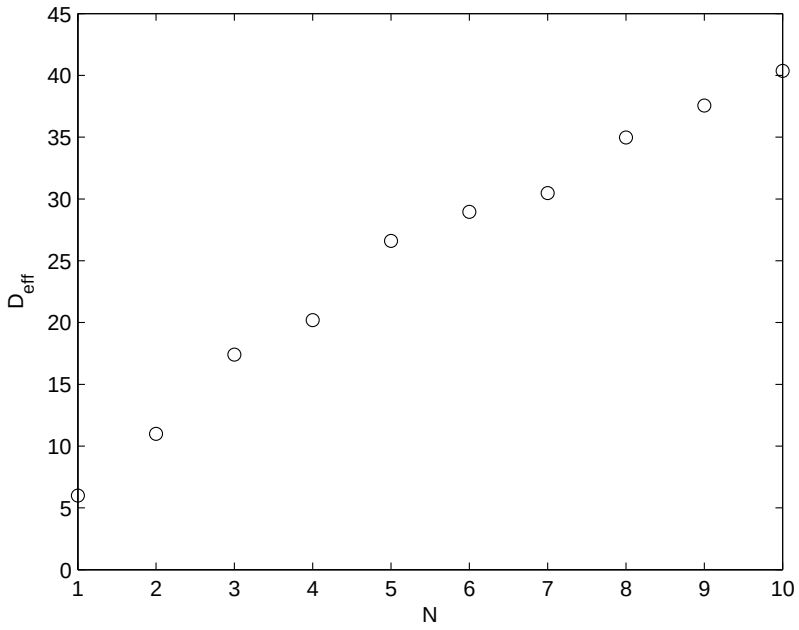

Figure 2.6: Effective dimensionality of the optimized pie phase plates with N slices [2].

from which the effective dimensionality can obviously only be calculated numerically. For $N = 2$ through $N = 10$, the angles α_n have been approximated by a Monte Carlo simulation [2]. The effective dimensionalities of these optimized phase plates are shown in figure 2.6. For $N = 1$ there is an analytical solution [13], $\alpha_1 = \pi/2$ or $3\pi/2$. In this case, eq. (2.16) reduces to

$$P_l = \begin{cases} \frac{1}{4}, & l = 0 \\ \frac{2}{\pi^2 l^2}(1 - \cos\frac{1}{2}\pi l), & l \neq 0, \end{cases} \tag{2.17}$$

which yields an effective dimensionality of 6. This means that its dimensionality is higher than that of the Heaviside phase plate (section 2.2) with $\phi = \pi$. Note that the latter is a special case of the pie phase plate with $N = 1$ and $\alpha_1 = \pi$.

3

The micro mirror array

The micro mirror array (MMA) is a chip with an array of mirrors that can be retracted individually while remaining parallel to each other. Thus the MMA can mimic the effect of any phase plate, changing the optical path length locally by reflection from a surface with an arbitrary height profile.

3.1 Characteristics

The individual mirror units are 40 μm $\times$ 40 μm in size and are placed in an array of 240 $\times$ 200, or 9.6 mm $\times$ 8.0 mm. Each mirror can be retracted a certain distance h, causing a phase shift of $4\pi h/\lambda$ in light of wavelength λ. The manual states that the maximum deflection of each micro mirror is $h = 320$ nm, meaning that a phase shift of 2π at the helium-neon wavelength ($\lambda = 632.8$ nm) can be achieved with just 4 nm to spare. Measurements indicate that the maximum deflection is slightly larger (see 4.6). The mirrors are controllable by an 8-bit D/A converter, meaning that there are 256 possible steps, each smaller than 2 nm.

Each mirror is connected to support posts by four hinges that act as springs. Its position is controlled by electrostatic attraction to individually addressable electrodes [15] (see figure 3.1). The mirrors do not occupy the entire 40 μm cell, as the hinges and the support posts take up some space (see figure 3.2). The entire surface is made of an aluminum alloy.

De Jong [4, pp. 19–21] measured interferometrically that the planarity of the MMA was about $\lambda/3$ or 211 nm, which is slightly worse than the specified value of $\lambda/5$.

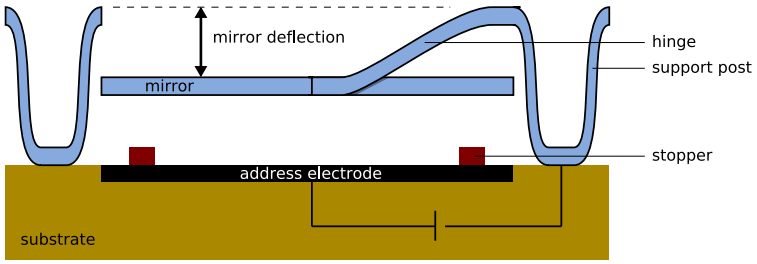

Figure 3.1: Schematic diagram of an individual micro mirror element (adapted from [15]).

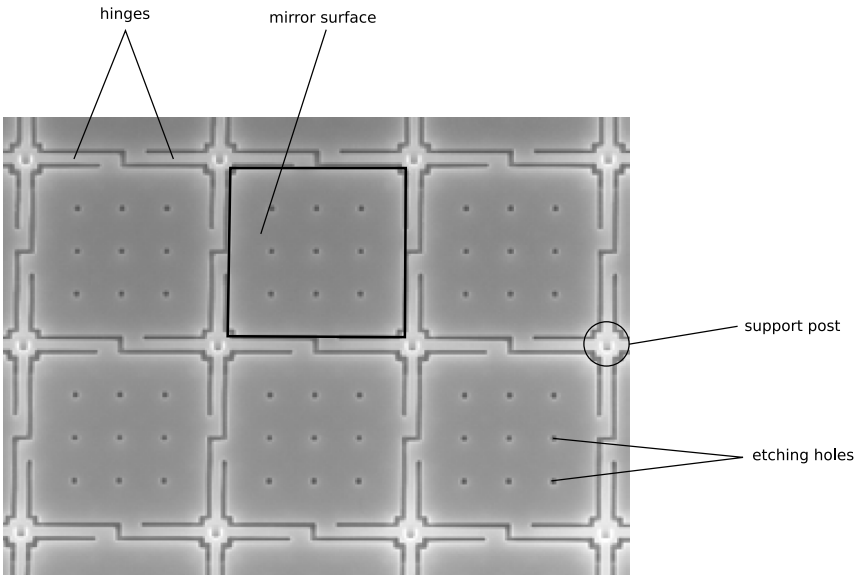

Figure 3.2: Image of the surface of several micro mirror elements (from [5, p. 6]).

The technology of such devices is still very much in development at the time of writing and this is exemplified by one practical problem that has not yet been solved. The mirrors cannot maintain their deflection constantly; instead they must be operated in a cycle, where $t_{\text{off}} \geq 17t_{\text{on}}$ and $1\,\text{ms} \leq t_{\text{on}} \leq 1\,\text{s}$, where t_{on} and t_{off} represent the time during which the mirrors can maintain their deflection, and the time in between deflections, respectively. This problem of limited on-time seemed at first to be the largest obstacle to the productive use of the MMA in an experiment.

3.2 Related software and hardware

The MMA is supplied with controller software, and can also be controlled through an ActiveX interface from any programming language that supports ActiveX. It was decided to write a LabVIEW controller program using the ActiveX interface, so that phase plates could be generated on the fly (which the existing controller software does not support). This way, it was also possible to control both the MMA and a camera using a single program.

LabVIEW turned out to be extremely suited to our goal. However, the latter was only partly achieved. The experiment started out using a CCD camera (Apogee Alta U1 model) which was completely controllable through an ActiveX interface. However, its CCD chip is covered by a glass window that introduces etalon effects at the helium-neon wavelength. Therefore, the Spiricon USB L320 beam profiler was used as a camera, but its ActiveX interface was slow when transferring large images, and it could not control the camera directly. The ActiveX interface could only control the camera through the software (LBA-USB) supplied with it. Therefore, functions available in LBA-USB were not duplicated in the LabVIEW program, since it was necessary to use both programs anyway.

The limited on-time problem can be circumvented by setting the camera's exposure time to t_{on} and triggering the exposure at the same time that the MMA's cycle starts. This was easily achieved using hardware: the MMA provides an output port that is set to High whenever a pattern is applied to the MMA and Low at all other times. This signal can simply be connected to the trigger input port of either camera.

Also, according to the Fraunhofer Institute for Photonic Microsystems, it is possible to deactivate a safety mode on the MMA which will allow on-times of up to two minutes, suitable for entanglement experiments where the entangled photons originate from the weak signal and idler beams of a down-conversion crystal. A two-minute on-time would require a recovery time of 34 minutes, but since the phase patterns can be programmed automatically using the MMA's LabVIEW interface, such an experiment could be run without human intervention.

	Apogee	Spiricon
Software	LabVIEW program, which controls both the camera and the MMA through their respective ActiveX interfaces.	LabVIEW program controlling the MMA, and supplied imaging software LBA-USB controlling the camera. A limited set of functions in LBA-USB can be controlled from LabVIEW.
Exposure time	10 ms–1 s (upper limit imposed by MMA)	1 ms–330 ms
Resolution	$768 \times 512 \times 16$ bits	$1616 \times 1216 \times 12$ bits
Pixel size	$9\ \mu\text{m} \times 9\ \mu\text{m}$	$4.4\ \mu\text{m} \times 4.4\ \mu\text{m}$
Required filter	10^{-4} ND (thick plate)	0.1 ND (attached to camera)
Triggering	3 V TTL input	3 V TTL input
Analysis	570 ms internal processing time at maximum image size. Fast data export to LabVIEW.	Width and intensity analysis of Gaussian-shaped beams; horizontal and vertical cross-sections. Fast internal processing time, but data export to LabVIEW very slow at maximum image size.
Other remarks	Cover glass causes etalon effects.	—

Table 3.1: Comparison of cameras used in imaging systems in combination with the MMA

3.3 Step-by-step introduction to the LabVIEW program

The definitive version of the LabVIEW controller program, `MMACameraController.vi`, was written for the Spiricon CCD camera. The Spiricon camera's software, LBA-USB, unfortunately makes it impossible to change certain settings automatically from outside the program. Therefore, this section will cover all the steps that must be taken to use the LabVIEW program along with LBA-USB to image the MMA.

The program starts with an initialization screen. The user can set the wavelength (in nm) of the laser light used to illuminate the MMA; the deflection heights of the phase plates are automatically calculated appropriate to the wavelength.

The setting "Exposure time" (in s) controls the on-time and off-time of the MMA. This setting must be set *separately* in LBA-USB. It is the unlabeled fifth control from the left on the top toolbar in LBA-USB and it is in ms. To check whether it is the correct control, hover the mouse over it; it will show a tooltip that says "Camera Exposure".

In order for the MMA drivers to work, the path to the chip configuration file must be specified in the appropriate field. This file is called `VC1583-03-02.ccf` and is installed along with the MMA drivers.

The camera settings, which cannot be controlled from the LabVIEW program, must also be correct. Aside from the exposure time, the resolution must be set and the triggering mode must be turned on. These settings are accessible from "Options" → "Camera..." in LBA-USB. Set the resolution with the drop-down menu labeled "Format" or customize it with the "xOffset, yOffset" and "Width, Height" boxes. Make

sure the "Input" box under "External trigger" is checked in order to put the camera into triggering mode.

The camera must be calibrated at the start of every experiment. Block the beam and press the "Ultracal!" button in LBA-USB's menu bar and the camera will automatically calibrate itself. Make sure the correct camera resolution and exposure time are set, because the camera must be recalibrated each time those settings are changed.

Press the "Start!" button in LBA-USB's menu bar to start capturing images. LBA-USB will wait for the trigger signal, so return to the LabVIEW program. The LabVIEW program's settings can be saved to a configuration file so that the user does not have to reset them every time he or she runs the program; additionally, checking the "Automatically load configuration from file" box before running the program will skip the initialization step altogether and run the program the last-*saved* (not last-used) settings. Press the OK button when finished with the settings.

The LabVIEW program's main interface will then appear (figure 3.3.) At upper left are the controls for selecting the deflection pattern (i.e., phase plate) to apply to the MMA. The pull-down menu at top lets the user choose between a constant phase plate, a Heaviside phase plate, a double Heaviside phase plate, a spiral phase plate, a pie phase plate, or an arbitrary phase plate in the form of a 240×200 BMP file, with 8-bit color.

The "Use calculated deflection distance" box allows the user to choose a phase difference other than π (for a Heaviside phase plate or a pie phase plate) or 2π (for a spiral phase plate). Checking the box will enable the "Path difference" control, which controls the height of the dislocation in said phase plates. The area below that contains controls specific to each type of phase plate. The controls appropriate to the phase plate currently selected in the pull-down menu are shown.

At lower left is the visual feedback from the MMA driver, showing the pattern that is currently programmed into the MMA. The phase plate data is not sent to the MMA until the user presses "Send to MMA". To switch between false color and grayscale displays, right-click on the MMA display and select the color scheme from the menu.

The four buttons in the box marked "Alignment phase steps" are for convenience during the alignment process. They send horizontally and vertically oriented Heaviside phase plates to the MMA, with a phase difference of π calculated for the appropriate wavelength, without having to press "Send to MMA".

Press "Download image" to transfer the current image in LBA-USB to the LabVIEW program. Be aware that this is slow at high resolutions. The image is then displayed at right. The graph below that displays a cross-section of the image, from the yellow cursor to the red cursor; drag the cursors and the cross-section will automatically update. To change the vertical scale of the cross-section, e.g. for examining the intensity

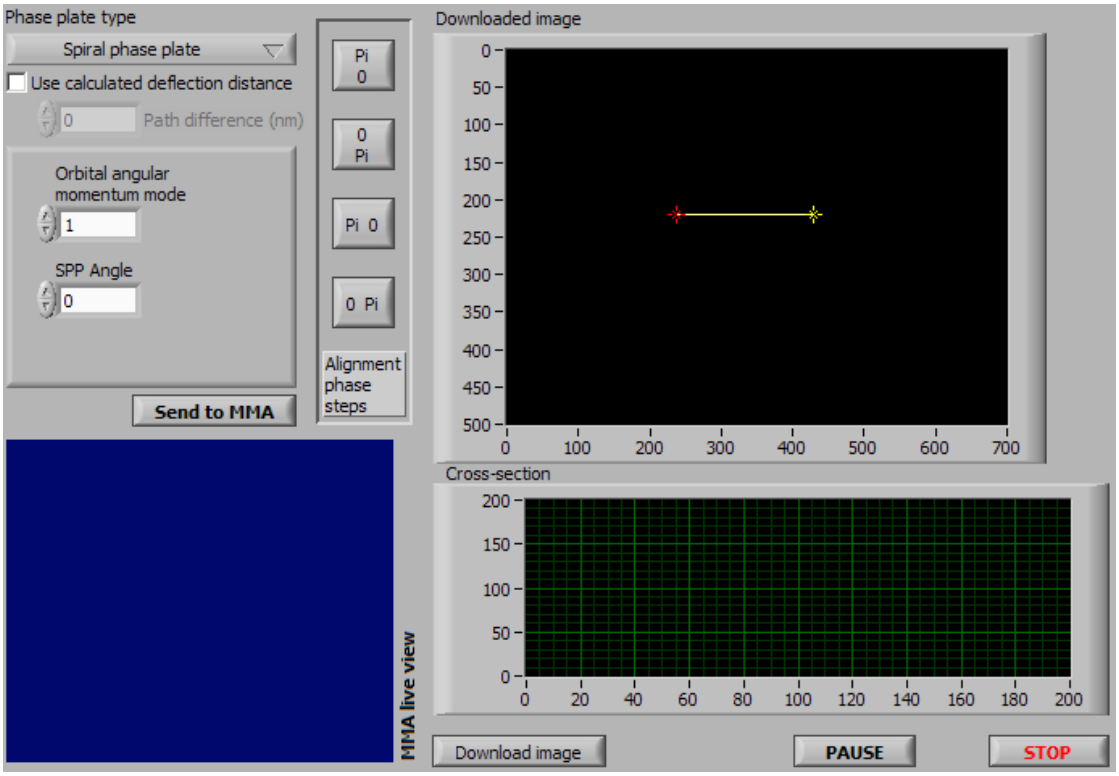

Figure 3.3: Screenshot of the LabVIEW program's main interface. The various elements are explained in the text.

minimum in a Heaviside phase plate pattern, click on one of the numbers on either end of the scale and type a new limit.

Press “Pause” to pause the MMA and “Stop” to shut it down. Do not abort the LabVIEW program without pressing “Stop”, or the MMA will not power down correctly.

4

Preliminary experiments

Although the primary goal of this work was to investigate the MMA's ability to mimic the phase plates described in chapter 2, many other experiments were carried out, either to gain a good understanding of the device's characteristics, or to investigate phenomena, such as diffraction effects, that came up in the course of other experiments. This chapter will discuss the experimental apparatus used; the effects of diffraction, polarization, and aliasing; and the practical concerns of aligning and calibrating the setup.

4.1 Far-field imaging setup

Most of the experiments described in this and the following chapter involved examination of the far field of a Gaussian beam the MMA. This was achieved with the experimental setup of figure 4.1. A helium-neon laser of wavelength $\lambda = 632.8\,\text{nm}$, with an output power of roughly 0.35 mW and a beam radius of $256 \pm 1\ \mu\text{m}$, was used to illuminate the MMA. The beam first passed through a variable beam expander (BE) set to $8\times$ magnification.

The beam expander was also used to collimate the beam, by fine-tuning one of its lenses. The beam's Rayleigh length was of the order of several meters, i.e. far longer than the beam's path through the experimental setup, ensuring that the phase front on the MMA was close to flat.

Three glass wedges (GW1–3) were used to steer and attenuate the beam. The first two were used to align the beam correctly on the MMA and GW3 was placed after all the

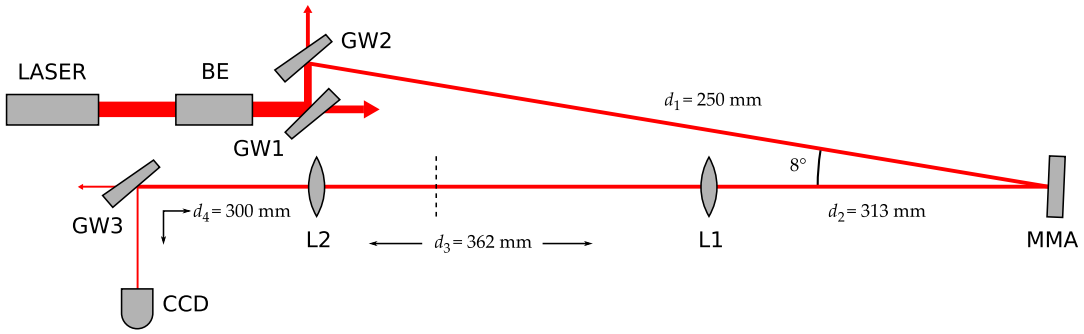

Figure 4.1: Far-field imaging setup. The width of the drawn laser beams roughly indicates their intensity relative to each other, but not to scale. Distances are also not to scale. The various elements of this setup are discussed in the text.

other components in order to be able to position the beam on the CCD camera. It was also advantageous to place GW3 last because the small amount of intensity reflected from it towards the camera was difficult to perceive with the naked eye, hindering alignment of any subsequent components.

The far-field imaging system consisted of two lenses. The first lens (L1), of focal length $f = 300$ mm, created an image of the far field of the MMA in its focal plane (indicated by a dotted line in figure 4.1). The second lens (L2), of focal length $f = 50$ mm, projected this image onto the camera with roughly $5\times$ magnification.

In order to build the imaging system correctly in spite of possible errors in the lenses' focal lengths, and uncertainty in the location of the CCD chip relative to the front of the camera, L2 was placed 300 mm away from the camera, which was placed at a fixed point. L1 was placed on a translation stage at approximately the correct distance from L2, and the translation stage was used to fine-tune the distance between L1 and L2 so as to minimize the diameter of the laser spot on the camera with the MMA off. In effect, L2's object distance was fixed and the translation stage was used to move L1's Fourier plane, in which the beam is focused most tightly, to coincide with it. The distance between the MMA and L1 was not critical, as long as it was greater than L1's focal length, because the beam entered L1 more or less parallel.

The 4° angle of incidence on the MMA caused a small extra phase difference compared with the case of normal incidence. This difference is only $1/\cos 4° - 1 \approx 0.2\%$ of the deflection height, and was therefore disregarded, because it is far less than the height difference between two steps on the MMA.

It was also discovered that the intensity of the laser could fluctuate up to 15% for some time after being turned on, due to the gain bandwidth shifting. In order to counteract

this effect, all data in this report were gathered after the laser had been running for at least 90 minutes, when the maximum fluctuation was found to be 3.6%.

It is useful to know the scale at which a displacement of the beam over the surface of the CCD chip corresponds to a distance on the surface of the MMA. In order to calculate this, we 'unfold' the optical axis between the MMA and the camera, disregarding the reflection from GW3, and use ray transfer matrices [14, pp. 26–36] to calculate:

$$\begin{bmatrix} x_{\mathrm{CCD}} \\ \theta_{\mathrm{CCD}} \end{bmatrix} = \begin{bmatrix} 1 & d_4 \\ 0 & 1 \end{bmatrix} \begin{bmatrix} 1 & 0 \\ -\frac{1}{f_2} & 1 \end{bmatrix} \begin{bmatrix} 1 & d_3 \\ 0 & 1 \end{bmatrix} \begin{bmatrix} 1 & 0 \\ -\frac{1}{f_1} & 1 \end{bmatrix} \begin{bmatrix} 1 & d_2 \\ 0 & 1 \end{bmatrix} \begin{bmatrix} x_{\mathrm{MMA}} \\ \theta_{\mathrm{MMA}} \end{bmatrix}, \quad (4.1)$$

where (x, θ) is the position and angle of a ray relative to the optical axis at a certain surface. Also, since x_{MMA} and θ_{MMA} are not independent, but controlled by the angle of GW2, $\theta_{\mathrm{MMA}} = \arctan x_{\mathrm{MMA}}/d_1$. Taking the small-angle approximation, we obtain $x_{\mathrm{MMA}} = 0.168 x_{\mathrm{CCD}}$. Stated simply, turning the adjustment knob of GW2's mount by one degree causes a displacement of 3.5 μm on the MMA, calculated using the distance between the knob and the fulcrum of the mount and the thread pitch of the knob. In practice, it is possible to align the beam with sufficient precision.

4.2 Diffraction effects

The MMA's mirrors form a two-dimensional periodic structure which causes the reflected light to diffract according to the grating equation. Figure 4.2 of De Jong [4, p. 18] shows a picture of the diffracted orders. We use the zero-order spot for our far-field images of phase plates.

When applying a uniform deflection (constant phase plate) to the MMA and examining the far field, it was discovered that the intensity of the spot varied according to the deflection height, exhibiting a minimum at slightly more than $\lambda/4$ deflection. The intensity 'missing' from the zero-order spot was found in the first and higher order spots. A conjectured explanation for this follows.

As described in 2.1, an ideal constant phase plate does nothing to the beam. However, the MMA is incapable of mimicking an ideal constant phase plate, because each mirror is connected to support posts by hinges, visible in figure 3.2. The support posts and the hinges are not at the same height as the mirrors and thus do not impart the same phase difference. In addition, the hinges tilt as the deflection increases, causing effects similar to a blazed grating [8, pp. 468–9]. See figure 4.2.

A field undergoing Fraunhofer diffraction from an arbitrary infinite periodic grating can be calculated using some elementary properties of the Fourier transform. Let us consider the grating's transmission function. The repeating structure, or unit cell, can be represented by a transmission function $H(x)$ on the interval $[-\frac{1}{2}a, \frac{1}{2}a]$, where a is

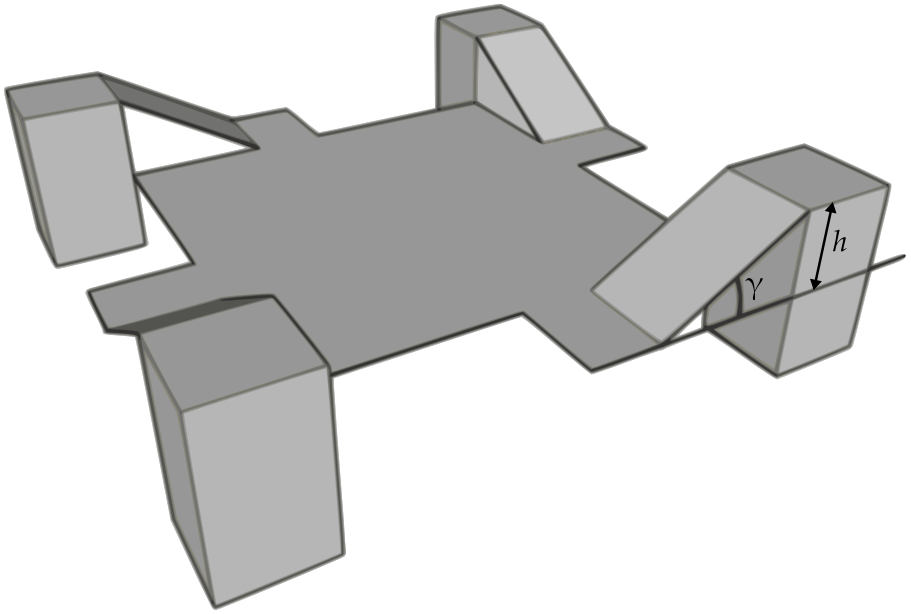

Figure 4.2: Exaggerated diagram of one micro mirror's deflection, with the blazing angle γ illustrated. The picture shows the mirror element, the support posts, and the hinges.

the grating period. The transmission function $G(x)$ of the entire grating consists of a repetition of this unit cell over the entire plane, with spatial period a. This repetition can be described mathematically by the convolution of $H(x)$ with a shah function[1] in which the spacing between the peaks is a:

$$G(x) = \text{Ш}(x/a) * H(x), \tag{4.2}$$

where $*$ denotes the convolution operation.

To obtain an expression for the far field, the incident field $E(x)$ is multiplied by the grating function $G(x)$ and Fourier transformed. By the Fourier transform's convolution theorem, the far field then consists of:

$$\begin{aligned} E_{\text{FF}}(X) &\propto \mathcal{F}\{E(x)\} * \mathcal{F}\{G(x)\} \\ &\propto \mathcal{F}\{E(x)\} * (\text{Ш}(aX) \cdot \mathcal{F}\{H(x)\}) \\ &\propto \mathcal{F}\{E(x)\} * \text{Ш}(aX)A(X). \end{aligned} \tag{4.3}$$

The shah function is its own Fourier transform, apart from scale. It represents the diffraction orders. The orders' relative amplitudes are determined by the diffraction

[1] We shall denote an infinite train of Dirac delta functions by the shah function, named after its similarity to the Cyrillic character Ш (*sha*): $\text{Ш}(x) = \sum_n \delta(x - n)$

envelope function $A(X) = \mathcal{F}\{H(x)\}$. Copies of the transform of $E(x)$ are repeated over all of the diffraction orders, at different intensities determined by the diffraction envelope. Hecht [8, pp. 451–3] derives a similar result using a diffraction integral.

In addition, the diffracting element in the unit cell can be blazed, i.e. its surface is tilted at an out-of-plane angle γ. A blazed grating does not change the position of the diffraction orders, but does shift the diffraction envelope so that its maximum no longer coincides with the zero-order spot [8, p. 469], by an angle of 2γ.

To illustrate this with an example, let us take the far field of a Gaussian, diffracted by an infinite number of infinitely long slits with width $2D$ and grating period a:

$$\begin{aligned} E_{\mathrm{FF}}(X) &\propto \mathcal{F}\left\{E_0 e^{-x^2/w^2} \cdot (\mathrm{Ш}(x/a) * \mathrm{rect}(x/D))\right\} \\ &= \frac{E_0 w}{\sqrt{2}} e^{-X^2 w^2/4} * \left(\frac{D}{a}\mathrm{Ш}(aX)\,\mathrm{sinc}(DX)\right). \end{aligned} \tag{4.4}$$

Here, rect denotes the rectangular function

$$\mathrm{rect}(t) = \begin{cases} 0, & |t| > \frac{1}{2}, \\ \frac{1}{2}, & |t| = \frac{1}{2}, \\ 1, & |t| < \frac{1}{2}, \end{cases} \tag{4.5}$$

and $\mathrm{sinc}(t) = \sin t/t$.

Continuing, we can express the parameters $(X, Y) = \frac{2\pi}{\lambda}(\sin\theta_x, \sin\theta_y)$ of the Fourier transform as a function of the angles θ_x, θ_y in the far field, in order to simplify the expressions involving the blazing angle γ. Using properties of the Fourier transform such as the shift theorem, we can write the far field of a reflection 'grating' composed of n separate rectangular components in a square unit cell of side a, as:

$$E_{\mathrm{FF}}(\theta_x, \theta_y) = \mathcal{F}\{E_{\mathrm{in}}\}(\theta_x, \theta_y) * \mathrm{Ш}\left(\frac{a\sin\theta_x}{\lambda}\right)\mathrm{Ш}\left(\frac{a\sin\theta_y}{\lambda}\right)\sum_n A_n(\theta_x, \theta_y). \tag{4.6}$$

Here, E_{in} is the incoming field. The shah functions determine the spacing of the diffracted orders. The amplitude function A_n is the diffraction envelope of each separate rectangular component of the unit cell, in its most general form:

$$\begin{aligned} A_n(\theta_x, \theta_y) = \frac{D_{xn} D_{yn}}{a^2} R_n e^{-i\phi_n} e^{-i(2\pi/\lambda)(x_n \sin\theta_x + y_n \sin\theta_y)} \\ \times \mathrm{sinc}\,\frac{\pi D_{xn}\sin(\theta_x - 2\gamma_{xn})}{\lambda}\,\mathrm{sinc}\,\frac{\pi D_{yn}\sin(\theta_y - 2\gamma_{yn})}{\lambda}. \end{aligned} \tag{4.7}$$

From left to right, the first factor $D_{xn}D_{yn}/a^2$ is the reflected fraction of the light from component n with dimensions D_{xn}, D_{yn}; R_n is the inherent reflectivity of the component; ϕ_n is any phase difference inherent to the component (such as the path difference

caused by the mirror's deflection); the next exponent is an extra phase factor due to the distance $\sqrt{x_n^2 + y_n^2}$ of the center of the component to the unit cell's origin; and the sinc functions are the actual diffraction envelope of the rectangular component, where γ_{xn}, γ_{yn} are the blazing angles in the x and y directions. This expression is summed over all n components of the unit cell. The unit cell's origin can be chosen arbitrarily, as long as it is the same for all components.

In order to apply the above derivation to the MMA, we must know the various dimensions of each cell, illustrated in figure 4.3. The length scale allows us to estimate the necessary dimensions of each component, shown beside the image. The hinges bend in some unknown fashion, and this must also be taken into account. In order to simplify the mathematics, they are modelled as if they cause some average phase difference proportional to the mirrors' phase difference, with proportionality constant $0 < \alpha < 1$, reflected in the factor $e^{-i\phi_n}$ in (4.7), where $\phi_H = \alpha\phi_M$. This parameter α has a large effect on the model and can only be determined empirically, lacking knowledge of how the hinges bend.

The reflectivity inherent to the MMA's material is assumed to be unity. Any other value results in a constant factor in (4.6) which is normalized later on, thus we need only concern ourselves with the relative reflectivities of the individual components. The support posts are not actually rectangular, but instead square with a circular hole in the center, but this is approximated by assigning them a reflectivity $R_P = P^2 - \pi r_P^2$. Lastly, to account for the etching holes in the mirror surface, the mirror is assigned a reflectivity $R_M = 0.98$. The reflectivity of the hinges, lacking holes or other features, remains unity.

Using these assumptions, along with what we know about the MMA's structure from its manual and [5], we can treat the MMA as an infinite two-dimensional reflection grating composed of $n = 6$ rectangular diffracting elements, four of which are blazed: the mirror surface, the support post, and four hinges. As figure 4.2 clearly shows, there is one hinge with its blazing angle pointing in each direction, causing the shift in the diffraction envelope to be symmetrical. The blazing angle γ is also a function of the deflection height h. We derive a complicated expression from (4.6) and (4.7) for the amplitude $A_{\mu\nu}$ of each diffraction order $\mu, \nu \in \mathbb{Z}$, by substituting the grating equation for θ_x and θ_y: $(\sin\theta_x, \sin\theta_y) = \frac{\lambda}{a}(\mu, \nu)$. The relative intensity $|A_{\mu\nu}|^2$ of each order is plotted in figure 4.4 for two deflection values, zero and $\lambda/4$.

It is clear that this model qualitatively predicts the shifting of intensity from the zero-order to the first and higher orders, just as measured. Intuitively, this is correct, because the blazed components reflect light at an angle away from the optical axis, which moves that light off to the side in the far field, and this effect depends on the deflection height.

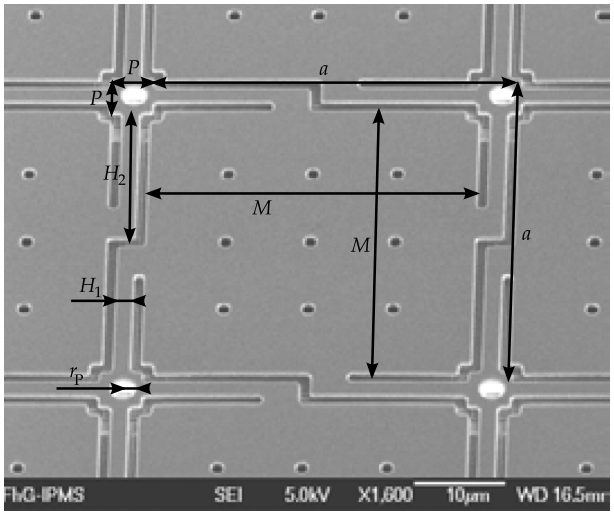

Dimension	Length (μm)
a	39.1
M	35.5
P	5.0
r_P	1.4
H_1	2.2
H_2	16.5

Figure 4.3: Relevant dimensions of a single micro mirror (original image from [5, p. 7]). This image is distorted (the mirrors are square) but the scale is correct if the dimensions are measured horizontally.

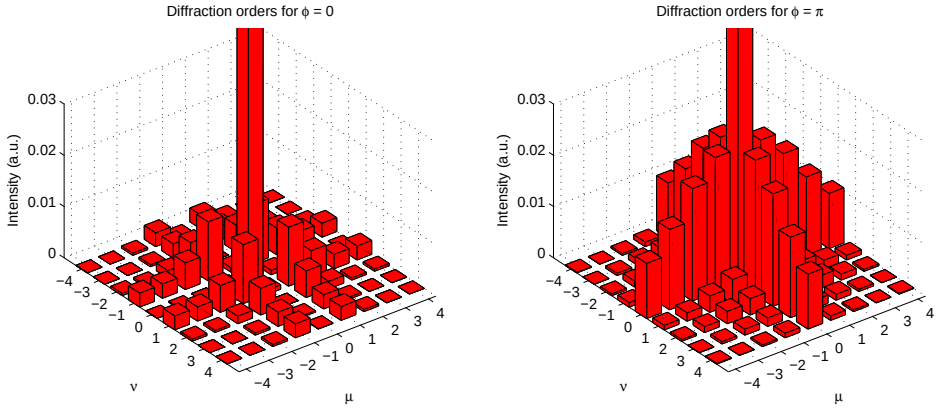

Figure 4.4: Relative intensity of diffraction spots calculated from (4.7) and plotted for horizontal and vertical orders $\mu, \nu = 0, \pm 1, \ldots, \pm 4$. At left is no deflection, at right a deflection of $\lambda/4$ causing a phase difference of π from the undeflected case. Both figures are normalized to the zero-order spot in the leftmost figure.

However, we are mainly interested in the zero-order intensity. For $\mu, \nu = 0$, the amplitude reduces to

$$A_{00}(h) = \frac{1}{a^2}\left(R_M M^2 + R_P P^2 e^{-i\phi(h)} + 4H_1 H_2 e^{-i\alpha\phi(h)} \operatorname{sinc} \frac{\pi H_2 \sin 2\gamma(h)}{\lambda}\right), \qquad (4.8)$$

where, as before, $\phi(h) = 4\pi h/\lambda$ and $\gamma(h) = \arctan h/H_2$.

We now assume that these diffraction effects scale down from the entire MMA and are valid for individual pixels. This assumption was validated by later measurements (see chapter 5.) We therefore introduce a quantity we call the effective reflectivity $\mathcal{R}$ of an MMA mirror. It represents the fraction of the intensity remaining in the zeroth order as a function of the deflection distance h. From (4.8) we write:

$$\mathcal{R}(h) = \frac{\left|R_M M^2 + R_P P^2 e^{-4\pi i h/\lambda} + 4H_1 H_2 e^{-4\pi i \alpha h/\lambda} \operatorname{sinc} \frac{2\pi h}{\lambda(1+h^2/H_2^2)}\right|^2}{(R_M M^2 + R_P P^2 + 4H_1 H_2)^2}. \qquad (4.9)$$

To test this expression and empirically determine a value for α, the intensity of the zero-order spot was measured for a series of constant phase plates. This measurement is plotted in figure 4.5, along with the theoretical model from (4.9) with α taken to be 0.65, based on the location of the minimum. A logical estimate of α is one-half, but figures 4.2 and 4.3 show that part of the hinges' length is attached to the side of the mirror. This probably makes the hinges' average distance from the mirror smaller, causing a slightly larger phase difference.

It seems that this model is a fair approximation of the effect. It does not fit the data perfectly; however, considering the assumption that the hinges do not curve as the mirror deflects and that the phase difference of the whole hinge is approximated by means of a single scalar parameter α, it predicts the effect surprisingly well.

4.3 Polarization effects

In order to measure the effect of the MMA on polarized light, two sheet polarizers were inserted into the setup of figure 4.1, one between GW2 and the MMA, and one between the MMA and L1. Their polarizing axes were oriented perpendicularly. In order to investigate whether reflection of light from the MMA influenced the polarization, both polarizers were examined at several angles, all perpendicular to each other. No light was transmitted, which was to be expected for crossed polarizers.

In a second experiment, a power meter was used to measure the beam power before and after the MMA, for several different angles of the first polarizer, to check whether the MMA's reflectivity was polarization-dependent. The ratio between the two was found to be approximately constant, suggesting that all polarizations were reflected equally from the MMA at a 4° angle of incidence.

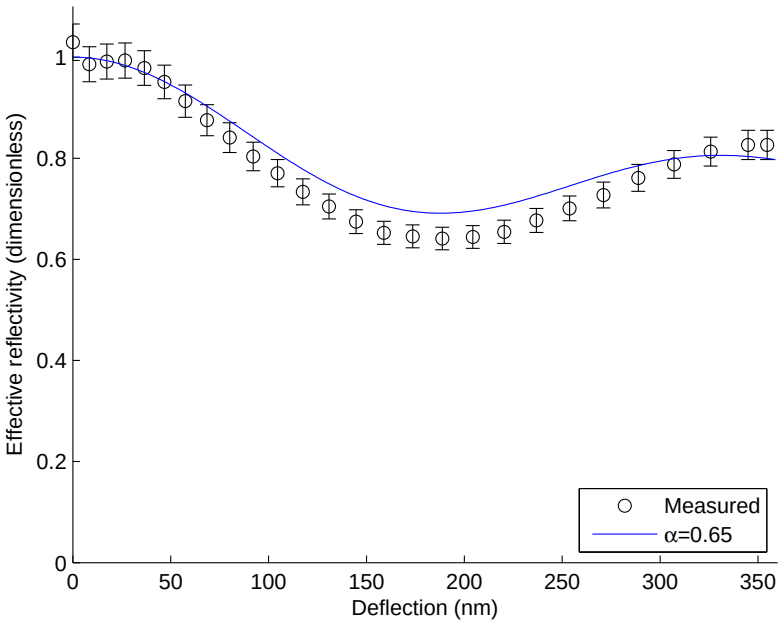

Figure 4.5: Effective reflectivity of a constant phase plate at $\lambda = 632.8$ nm as a function of its deflection.

4.4 Aliasing effects

The MMA is composed of discrete elements, similar to pixels on a computer screen. Straight lines that are not perfectly horizontal or vertical undergo aliasing when drawn on a grid of pixels, visible as a 'stepping' effect. De Jong [4, pp. 23–24] tested whether aliasing caused any discernible effects on a Heaviside phase plate oriented at 45°; it did not. However, aliasing effects become worse for decreasing angles between step and grid lines, and mimicking a pie phase plate on the MMA requires lines of all different angles.

The images in figure 4.6, of the far field of a Heaviside phase plate at 0° and 1° orientation, suggest that there were no discernible aliasing effects even at fairly small angles. The shape of both images is the same, and the intensity differs by only 0.3%. The only difference is that the pattern was rotated 1°. This suggests that aliasing only becomes a problem when the angle and the beam radius are both small enough that only a limited number of 'steps' are illuminated by the beam. This happens in pie phase plates with a large number of slices (see 5.2), because the smallest slices are less than one pixel wide close to the center.

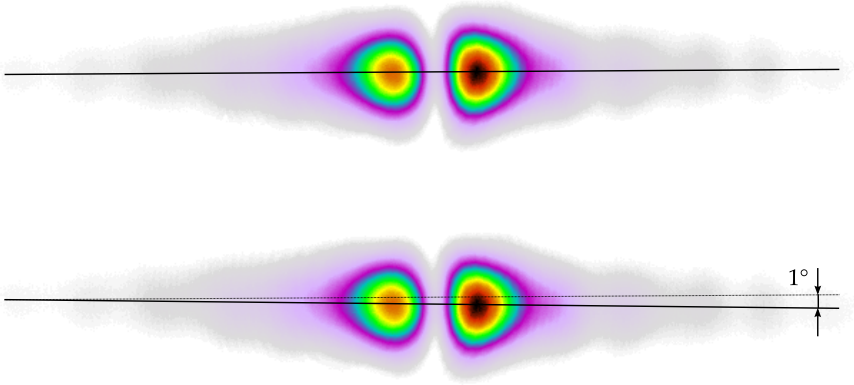

Figure 4.6: Comparison of Heaviside phase plates at 0° and 1° orientation.

4.5 Alignment

The simplest way to align the laser spot on the MMA is to use a Heaviside phase plate (section 2.2). If we calculate the far field of an ideal Heaviside phase plate of phase step π that is not aligned to the center of the incoming Gaussian beam, we find that the peaks remain equal, while the minimum between the peaks becomes more than zero. If, on the other hand, the phase step is not equal to π, but the system is aligned perfectly, the minimum remains zero, and the peaks become unequal. Figure 4.7 shows each of these cases. Thus, it is relatively simple to align a perfect Heaviside phase plate by bringing the minimum to zero.

However, as we have seen before, the MMA's diffraction effects cause the effective reflectivity (4.9) of the deflected side of the Heaviside phase plate to be less than that of the undeflected side. This changes the transfer function of the Heaviside phase plate to

$$H(x) = \begin{cases} 1, & x < 0 \\ \mathcal{R}e^{-i\phi}, & x \geq 0, \end{cases} \tag{4.10}$$

and, by the same method as in appendix A.1, the far field is calculated to be:

$$I_{\mathrm{FF}}(X,0) \propto 2\pi w^4 |E_0|^2 \left(\frac{\pi}{4} (\tfrac{1}{2} + \tfrac{1}{2}\mathcal{R}^2 + \mathcal{R}\cos\phi) e^{-2\pi^2 w^2 X^2} \right.$$
$$\left. - \mathcal{R}\sqrt{\pi}\sin\phi\, e^{-\pi^2 w^2 X^2} D(\pi w X) + (\tfrac{1}{2} + \tfrac{1}{2}\mathcal{R}^2 - \mathcal{R}\cos\phi)(D(\pi w X))^2 \right). \tag{4.11}$$

The minimum of this far-field distribution is *no longer* at its lowest point when the beam is aligned to the center of the Heaviside phase plate. In addition, the curvature of the MMA surface (section 3.1) causes the intensity of the peaks to vary according to

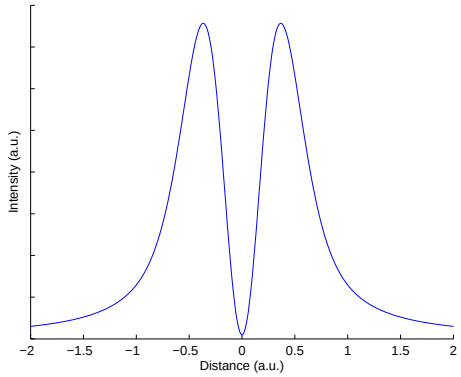

(a) Perfect Heaviside phase plate, symmetrically illuminated

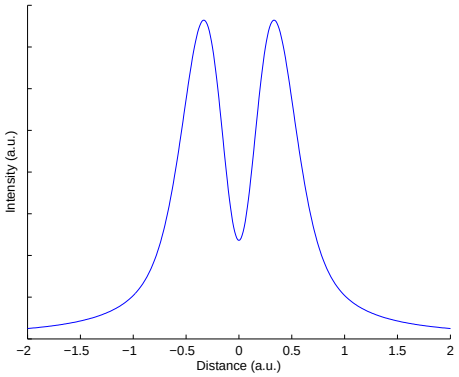

(b) Perfect Heaviside phase plate, asymmetrically illuminated

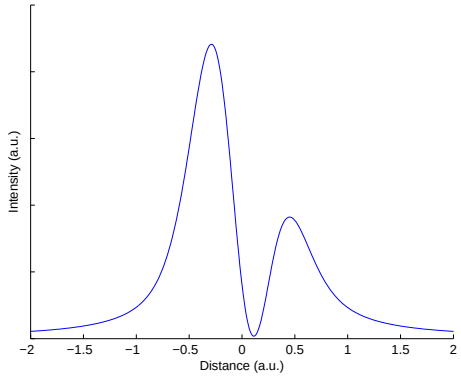

(c) Imperfect (i.e. phase step not equal to π) Heaviside phase plate, symmetrically illuminated

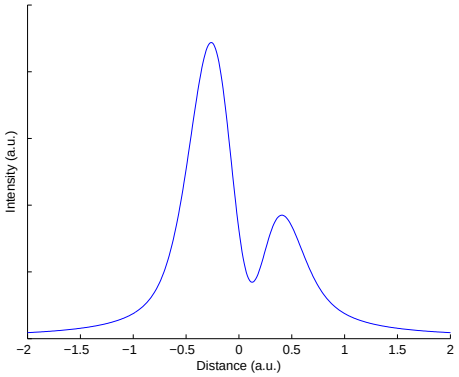

(d) Imperfect Heaviside phase plate, asymmetrically illuminated

Figure 4.7: Cross-sections of the far-field intensity distributions of a Gaussian beam which has passed various imperfect Heaviside phase plates.

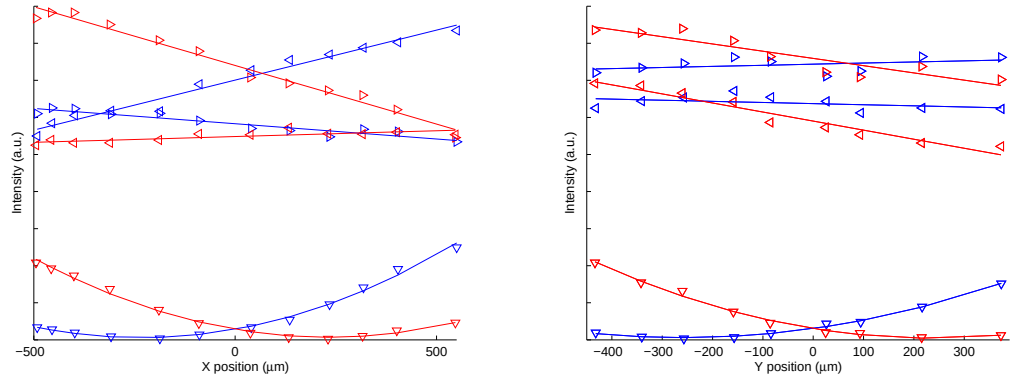

(a) Horizontal (b) Vertical

Legend: Blue, normal; red, mirrored; ▽, minimum; ◁, left or top peak; ▷, right or bottom peak.

Figure 4.8: Relative intensities of peaks and minima of horizontally and vertically oriented Heaviside phase plate patterns. These figures were created by applying Heaviside phase plate patterns to the MMA and shifting the beam in a direction perpendicular to the phase dislocation, recording the intensities of the peaks and minima in the far field. The horizontal axis indicates the position of the beam center on the MMA relative to the step, and the solid lines are a guide to the eye.

where the beam is located on the surface. However, if the beam is perfectly aligned, the far-field intensity distribution will be mirrored when the phase plate pattern is mirrored. The center of the phase plate pattern, i.e. the dislocation, remains at the same place on the MMA and therefore undergoes the same curvature effects. Therefore, if the minimum between the two peaks remains at the same intensity when the pattern is mirrored, then the beam is well-aligned.

This is illustrated in figure 4.8 for vertically and horizontally oriented Heaviside phase plates of phase step $\phi \approx \pi$. The peak intensities differ from the theory because of the curvature of the MMA surface, but it is readily apparent at which point the beam is aligned by examining the minimum intensity at the center. Note that the vertical curvature is apparently far worse than the horizontal curvature, since in figure 4.8a the pattern is approximately mirrored, but in figure 4.8b the bottom peak is always more intense than the top peak.

This process can be carried out separately for vertically and horizontally oriented Heaviside phase plates. It may be possible to align the beam with a 'double Heaviside phase plate' in which two diagonally opposite quadrants are deflected by $\lambda/4$, but in practice it is easier to separate the vertical and horizontal alignment.

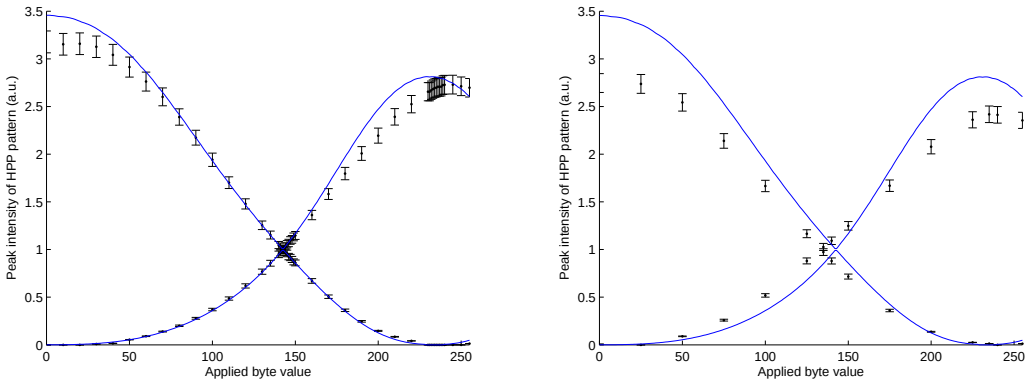

(a) Horizontal (b) Vertical

Figure 4.9: Relative intensities of Heaviside phase plate peaks as a function of the address value of the deflected half. The solid line indicates the theoretical model of (4.11). Compare to figure 4.7c.

4.6 Calibration of the MMA

In order to get any useful results from the far-field images, it was necessary to find out exactly how the address byte of a single MMA cell related to the physical deflection distance. De Jong [4, pp. 22–23] found an address value of 137 to correspond to a deflection of $\lambda/4$ or 158 nm, but the far-field behavior of the phase patterns, due to the effects described in the preceding sections, was more complicated than assumed there, and thus required more investigation.

It is evident from cursory examination that the scale between the address value and the deflection distance is not linear. Figure 2 of [6] shows what seems to be a quadratic correspondence between address *voltage* and deflection.

To confirm this, the intensities of the two peaks of the far-field intensity pattern were measured for Heaviside phase plates with phase steps over the entire range of address values, 0–255. Because of the curvature of the MMA and the uncertainty of how accurate the model of (4.11) is, there are only three points on which we can base our calibration: zero; $\lambda/4$, where the peaks are equal; and $\lambda/2$, where the far field becomes Gaussian in approximation. Figure 4.9 shows the results for horizontally and vertically oriented Heaviside phase plates. Since we concluded in 4.5 that the vertical curvature was far worse than the horizontal curvature, we only use figure 4.9a for the determination of these points.

The deflection distance of $\lambda/4 = 158.2$ nm lies between address values 142 and 143. Based on the possible error in alignment, we assign this value an error of ± 3. By

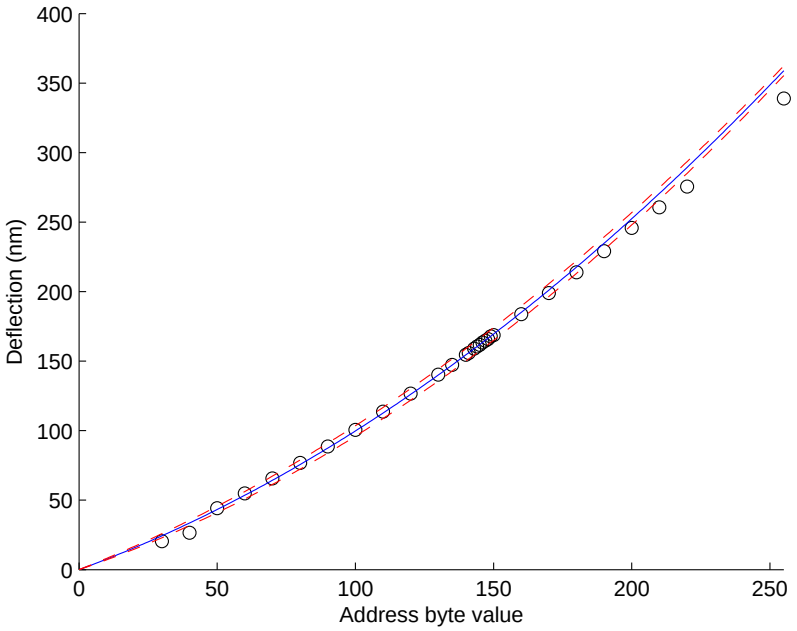

Figure 4.10: Calibration curve for the MMA. The solid line is given by (4.12) and the dotted lines indicate the error margin. The circles are estimates calculated from the ratios of the peaks in figure 4.9a. They become increasingly inaccurate away from the center because the effect of the MMA's curvature is ignored.

examining the correlations of intensity distributions of the address values around $\lambda/2$ to a Gaussian curve, we determine that a deflection distance of $\lambda/2 = 316.4$ nm corresponds to an address value of 234 ± 2. The maximum deflection is apparently around 360 nm and not 320 nm as stated in the manual.

Fitting this to a curve of the form $h(n) = an^2 + bn$ yields:

$$\left.\begin{array}{rcl} a & = & 2.644 \times 10^{-12} \text{ m} \\ b & = & 7.334 \times 10^{-10} \text{ m} \end{array}\right\}. \tag{4.12}$$

See figure 4.10, where the deflection of the other values was determined by the model of (4.11). The error margin calculated from the error margins in a and b is illustrated with a dotted line. The maximum error at any point on the curve is 4.5×10^{-9} m.

The relation between address value and deflection distance seems to be approximated well by a quadratic, but it is completely different from figure 2 of [6] and figure 9 of [15]. We suspect that some sort of correction is applied inside the MMA controller which makes the relation almost, but not quite, linear.

5

Experimental phase plate results

The ultimate goal of this research is to examine the quality of complicated angular phase plates, such as spiral and pie phase plates, as mimicked by the MMA. Examining the far-field intensity distribution of a Gaussian beam after reflection from the MMA and comparing it to the calculated distribution can provide some qualitative idea of whether the MMA is a good substitute. It can also give a good indication of the MMA's most significant shortcomings.

All of the figures in this chapter have their own normalized intensity scale, except for figures 5.5a–l, which all have the same scale. Occasionally the scale was modified to bring out certain details. The color scale is shown in figure 5.1.

5.1 Spiral phase plate

Figure 5.2 shows the intensity distributions of ideal Gaussian beams after passing ideal spiral phase plates. Figures 5.2a–e are of phase plates with integer vorticity, calculated analytically from eq. (2.13) which was derived in appendix A.2. Figures 5.2f–i are of phase plates with half-integer vorticity, calculated numerically by a discrete Fourier transform of the near field.

Figure 5.1: Color scale used in figures showing an intensity distribution.

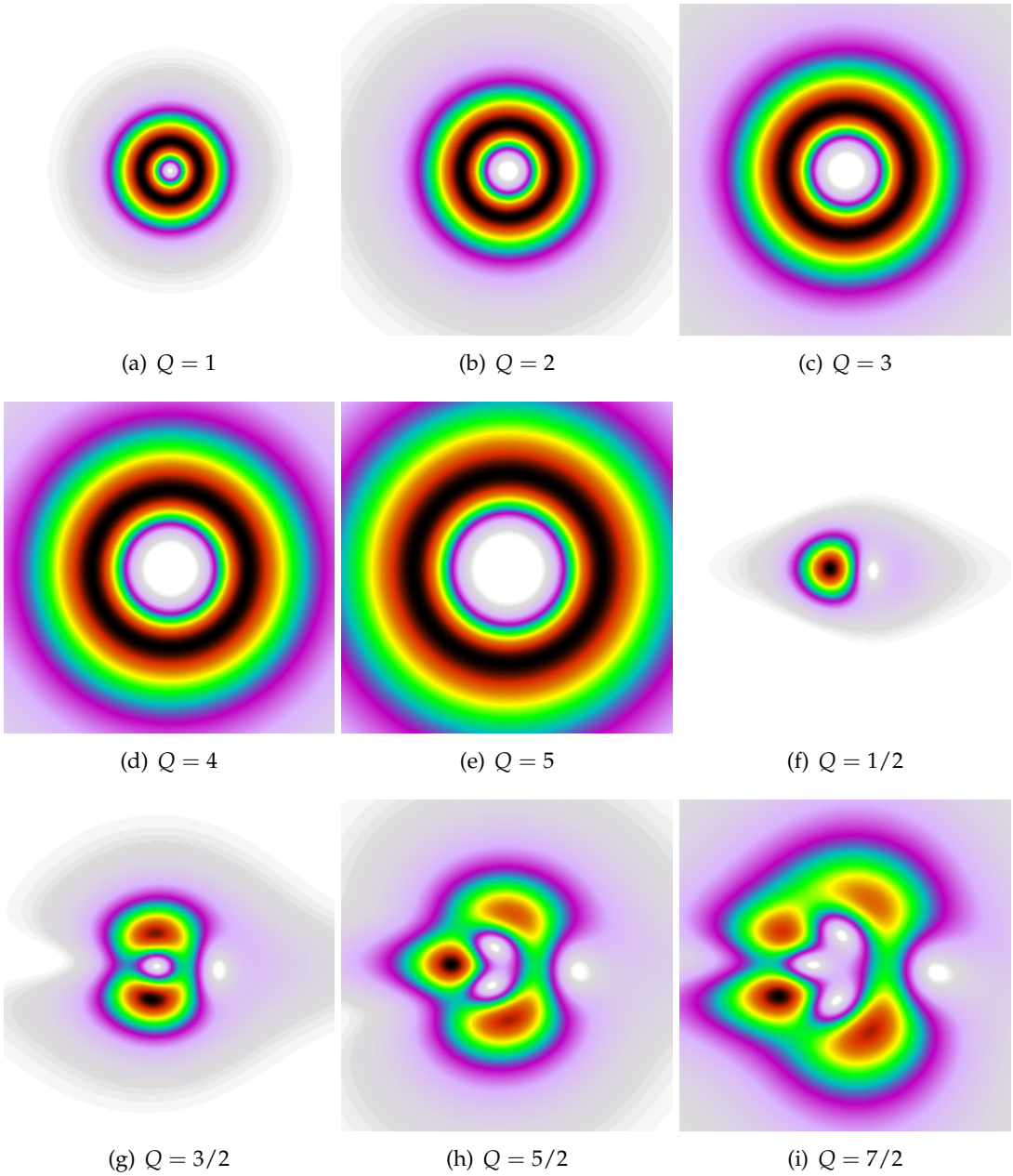

(a) $Q = 1$ (b) $Q = 2$ (c) $Q = 3$

(d) $Q = 4$ (e) $Q = 5$ (f) $Q = 1/2$

(g) $Q = 3/2$ (h) $Q = 5/2$ (i) $Q = 7/2$

Figure 5.2: Calculated far field intensity distributions of a Gaussian beam having passed an ideal spiral phase plate with vorticity Q.

Figure 5.3 shows the same intensity distributions, adapted for the MMA by taking into account the effective reflectivity of each MMA mirror as a function of its deflection (4.9). All of these figures were calculated numerically by discrete Fourier transform. Of special note is that the intensities of figures 5.3a–e are no longer strictly radial functions.

The measurements corresponding to figures 5.2 and 5.3 are shown in figure 5.4. Spiral phase plate patterns, with their heights corrected according to (4.12), were applied to the MMA, and the results are qualitatively quite similar to figure 5.3. This supports the assumption of section 4.2 that the diffraction effects which cause the effective reflectivity scale down from the MMA to an arbitrarily small number of pixels.

The most significant difference exhibited between the calculations of figure 5.3 and the measurements of figure 5.4 is especially evident in the integer-vorticity phase plates: there seem to be brighter areas on the 'northeast-southwest' axis and dimmer areas on the 'northwest-southeast' axis.

Figure 5.5 shows the effects on the far field intensity when the $Q = 1$ plate was rotated. The MMA itself remained stationary. The expectation was a simple rotation of the pattern of figure 5.3a. However, the brighter and darker areas remained in the same place, demonstrating that they were not caused by the MMA's deflection, but were inherent to the stationary MMA itself. Therefore, they are believed to be a consequence of the MMA's curvature.

5.2 Pie phase plate

Figure 5.6 shows the far field intensity distributions of ideal Gaussian beams after passing ideal pie phase plates with N slices, calculated analytically from (A.21). Figure 5.7 shows the same, but with the lowered effective reflectivity of the sections with phase difference π taken into account, and calculated numerically by discrete Fourier transform. It is apparent that the intensity at the center of each figure in 5.7 is far greater than in figure 5.6. This is a consequence of the sections with phase difference π reflecting less light to interfere with the light reflected by the undeflected sections.

The measurements corresponding with figure 5.7 are shown in figure 5.8. Disregarding the effect of the MMA's curvature, which makes them look slightly off-center, they look remarkably like their theoretical counterparts.

Unlike the spiral phase plate, the effective reflectivity problem can be corrected in a pie phase plate. Adding a constant deflection to the entire pattern does not change the far field, or the phase of any part of the beam relative to another, so we are free to choose any two address values to represent zero and π, as long as their deflection heights

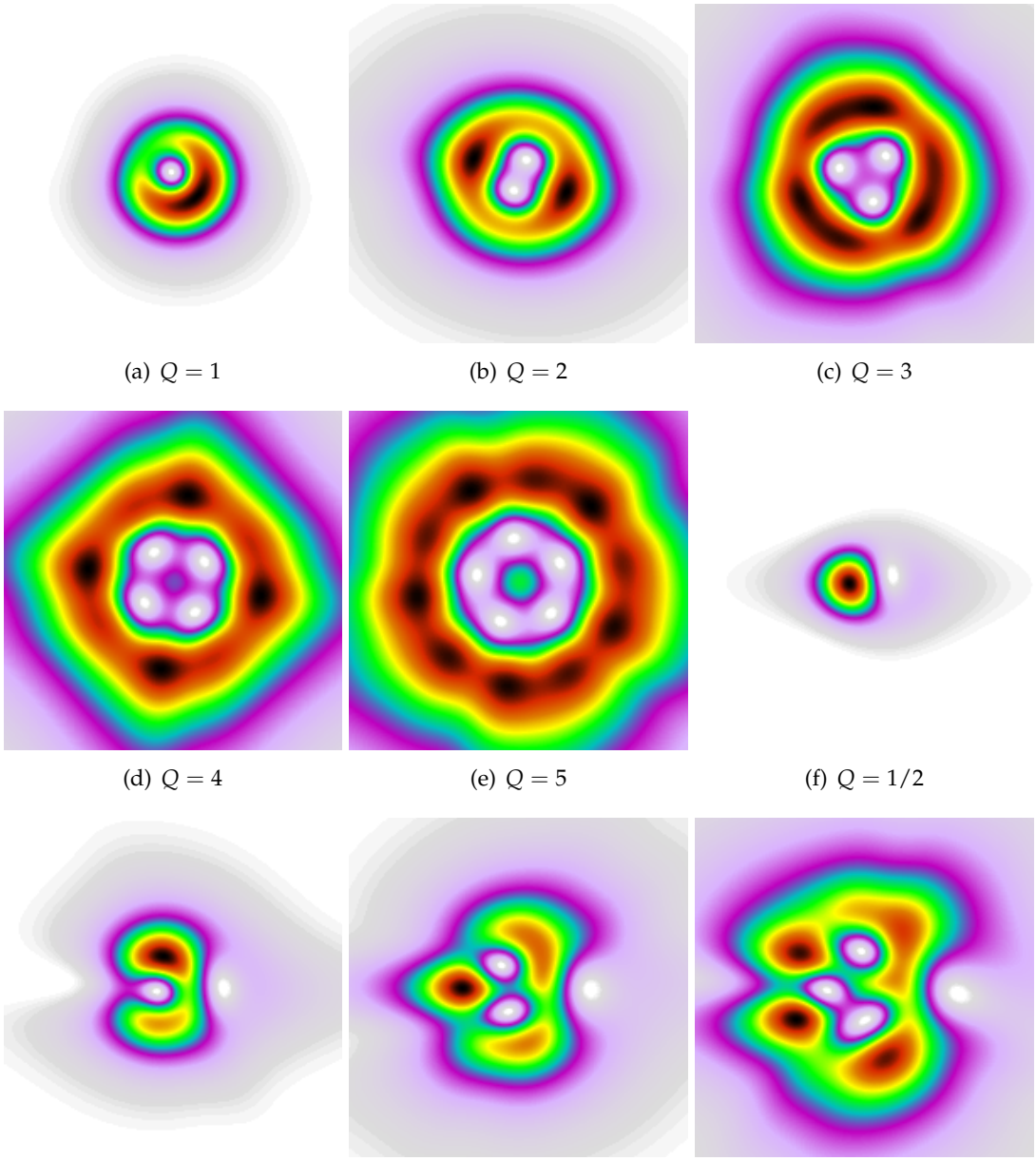

(a) $Q = 1$ (b) $Q = 2$ (c) $Q = 3$

(d) $Q = 4$ (e) $Q = 5$ (f) $Q = 1/2$

(g) $Q = 3/2$ (h) $Q = 5/2$ (i) $Q = 7/2$

Figure 5.3: Calculated far field intensity distributions of a Gaussian beam having passed a spiral phase plate with vorticity Q and a height-dependent effective reflectivity. Here, the intensity has a slight angular dependence instead of being a purely radial function as in figure 5.2.

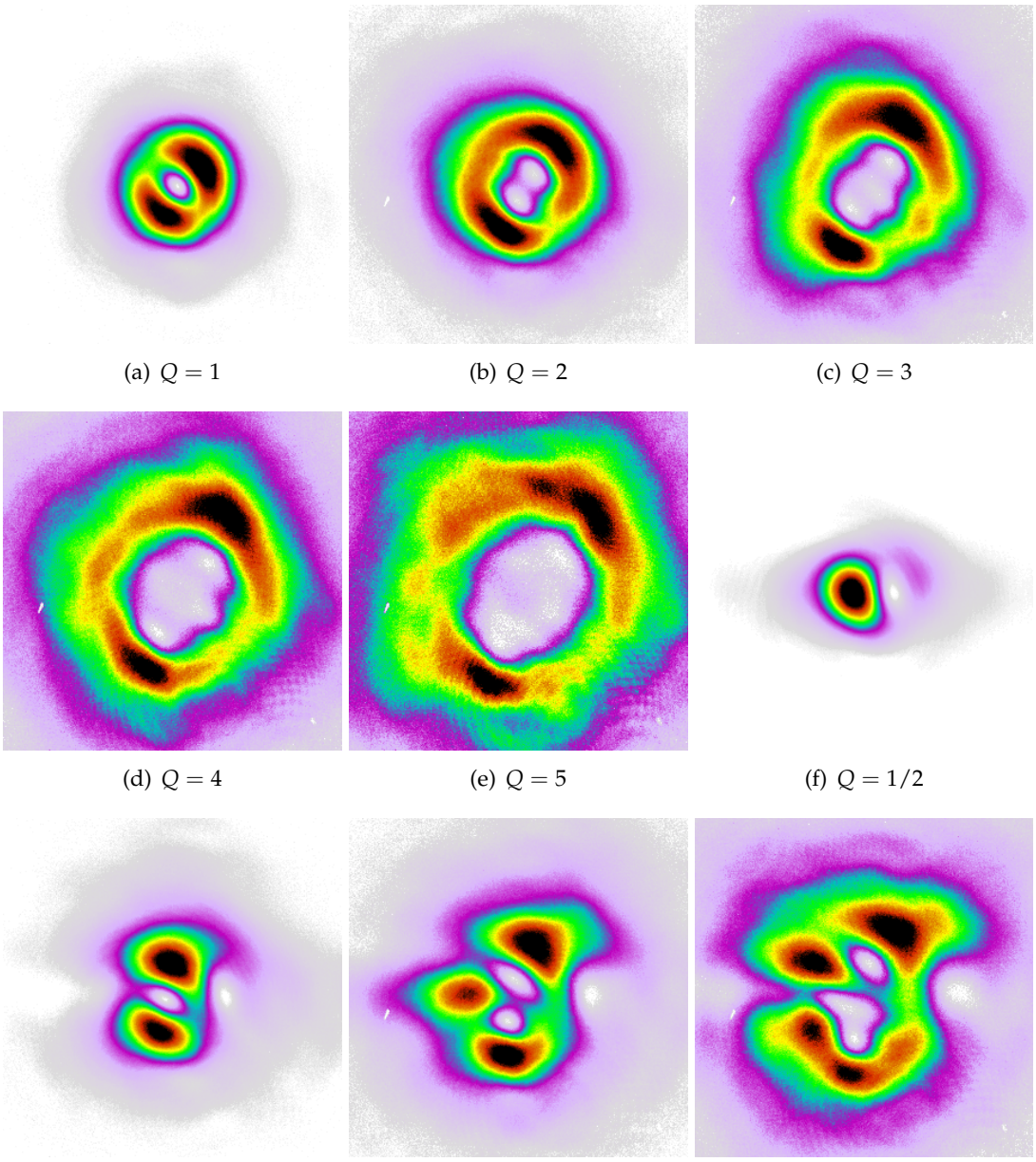

(a) $Q = 1$ (b) $Q = 2$ (c) $Q = 3$

(d) $Q = 4$ (e) $Q = 5$ (f) $Q = 1/2$

(g) $Q = 3/2$ (h) $Q = 5/2$ (i) $Q = 7/2$

Figure 5.4: Measured far field intensity distributions of a Gaussian beam having passed a spiral phase plate with vorticity Q. These images agree well with figure 5.3 except for the dimmer areas on the 'northwest-southeast' axis.

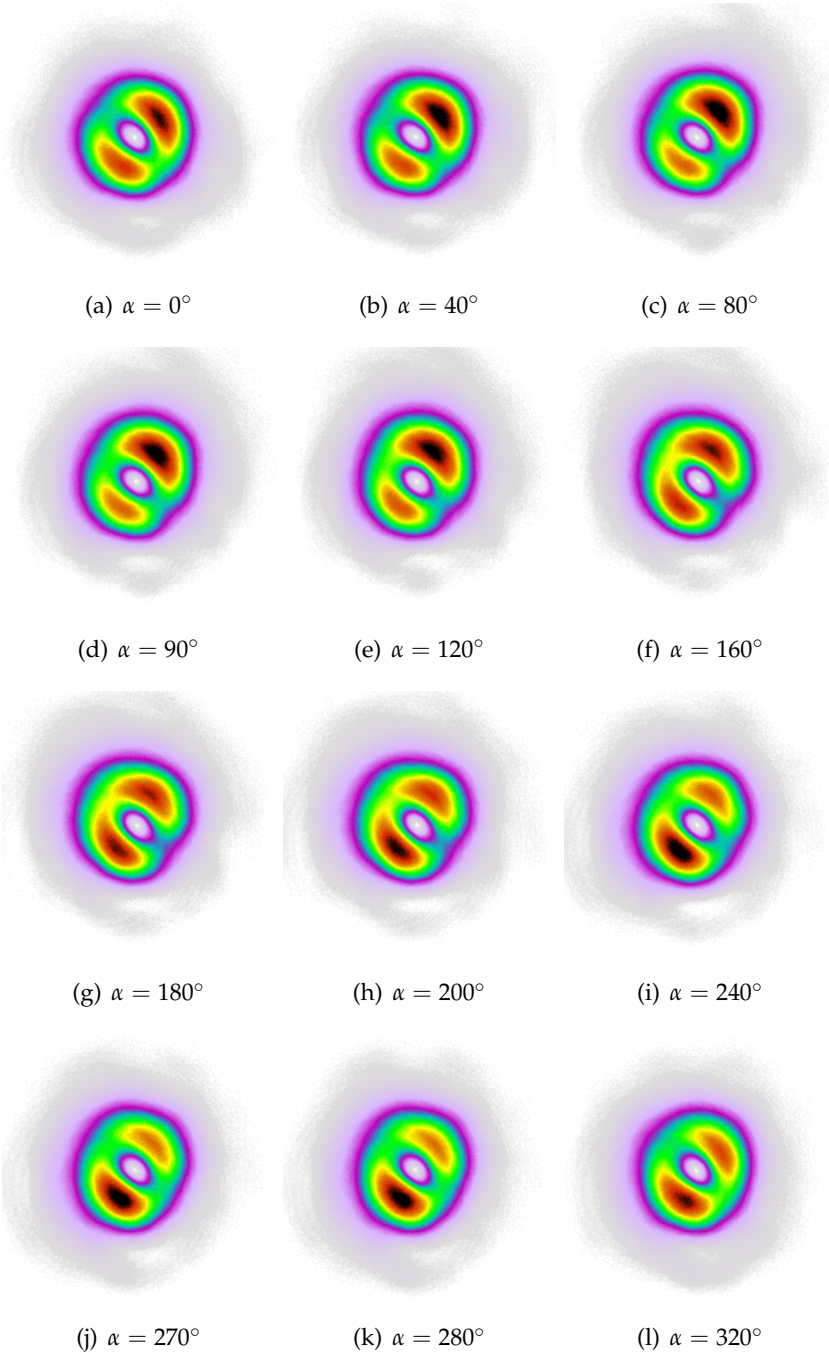

(a) $\alpha = 0°$ (b) $\alpha = 40°$ (c) $\alpha = 80°$

(d) $\alpha = 90°$ (e) $\alpha = 120°$ (f) $\alpha = 160°$

(g) $\alpha = 180°$ (h) $\alpha = 200°$ (i) $\alpha = 240°$

(j) $\alpha = 270°$ (k) $\alpha = 280°$ (l) $\alpha = 320°$

Figure 5.5: Measured far field intensity distributions of a Gaussian beam having passed a $Q = 1$ spiral phase plate oriented at an angle α. This shows that the dimmer areas on the 'northwest-southeast' axis are a feature of the mirror surface and not of the phase pattern.

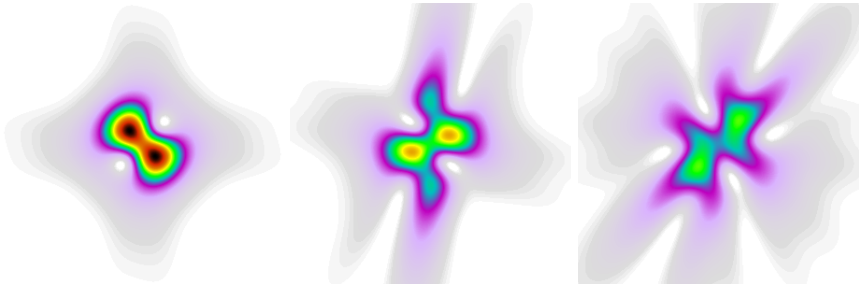

(a) $N = 1$ (b) $N = 2$ (c) $N = 3$

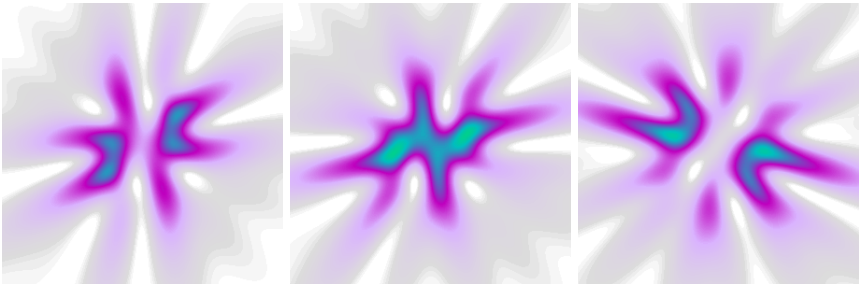

(d) $N = 4$ (e) $N = 5$ (f) $N = 6$

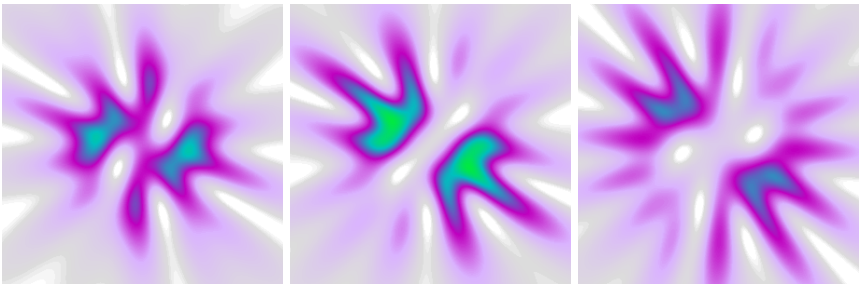

(g) $N = 7$ (h) $N = 8$ (i) $N = 9$

(j) $N = 10$

Figure 5.6: Calculated far field intensity distributions of a Gaussian beam having passed an ideal pie phase plate with N slices.

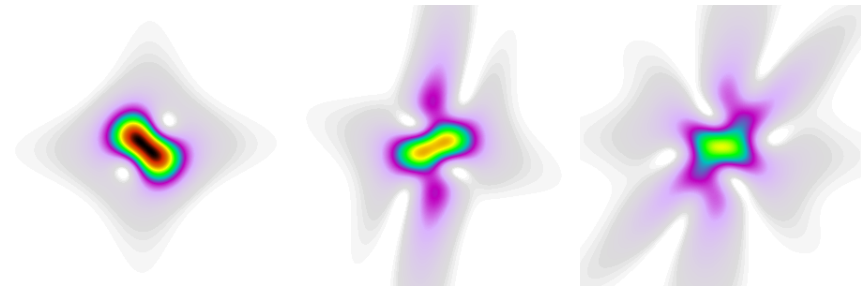

(a) $N = 1$ (b) $N = 2$ (c) $N = 3$

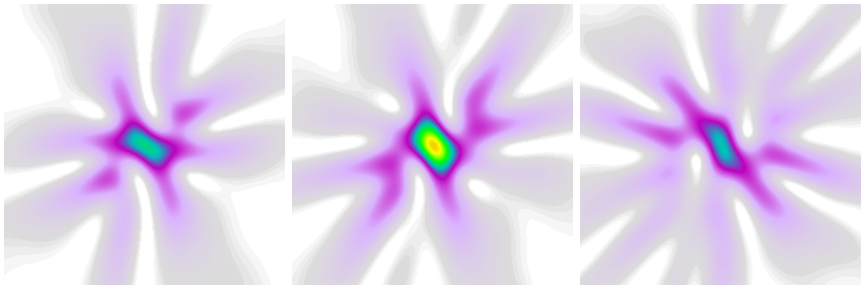

(d) $N = 4$ (e) $N = 5$ (f) $N = 6$

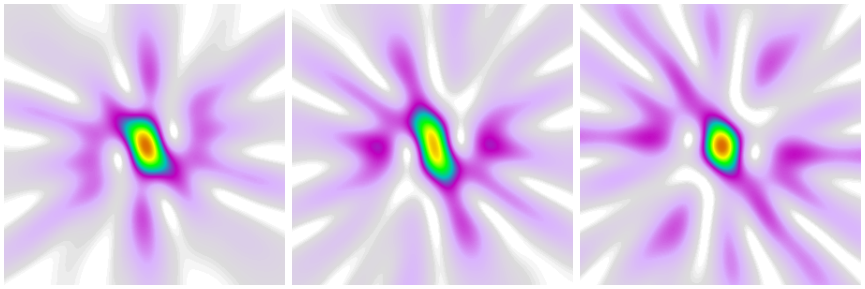

(g) $N = 7$ (h) $N = 8$ (i) $N = 9$

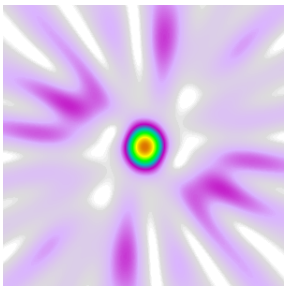

(j) $N = 10$

Figure 5.7: Calculated far field intensity distributions of a Gaussian beam having passed a pie phase plate with N slices and a height-dependent effective reflectivity, i.e. $\mathcal{R}_{\phi=0} > \mathcal{R}_{\phi=\pi}$.

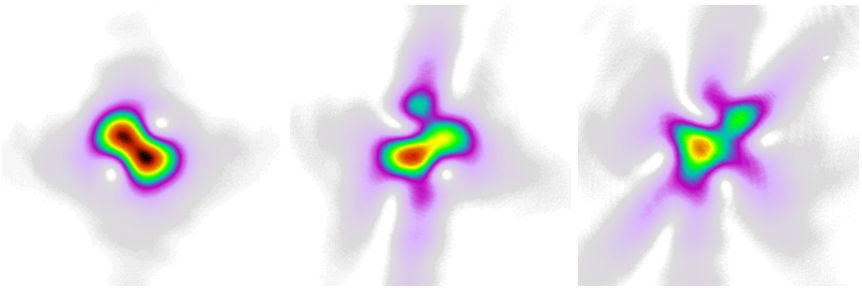

(a) $N = 1$

(b) $N = 2$

(c) $N = 3$

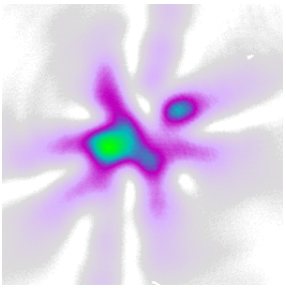

(d) $N = 4$

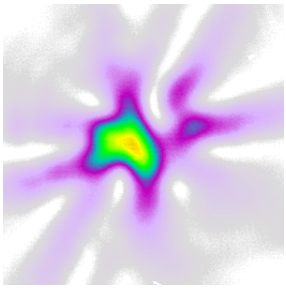

(e) $N = 5$

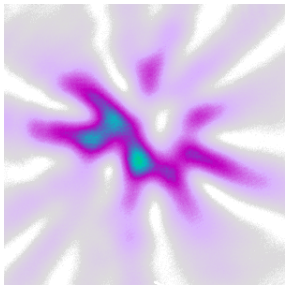

(f) $N = 6$

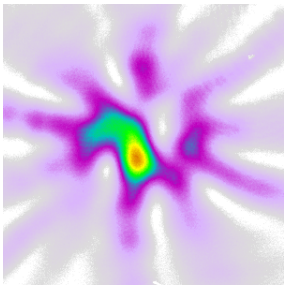

(g) $N = 7$

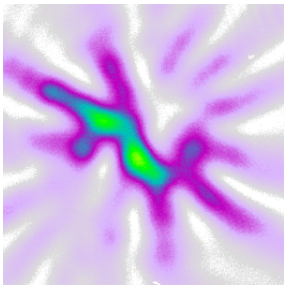

(h) $N = 8$

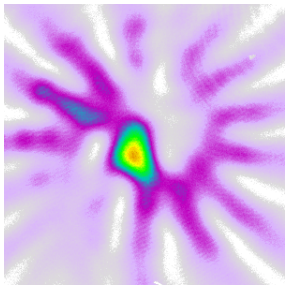

(i) $N = 9$

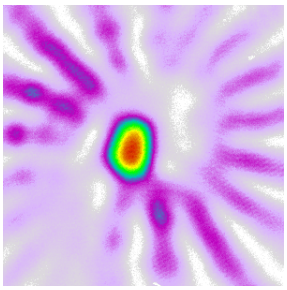

(j) $N = 10$

Figure 5.8: Measured far field intensity distributions of a Gaussian beam having passed a pie phase plate with N slices, where the effective reflectivity of the sectors with phase 0 and π is not equal. Compare figure 5.7.

differ by $\lambda/4$. Figure 4.5 shows that there must be a combination of two deflection heights at which the effective reflectivity is equal.

Figure 5.9 shows the same measurements again, with a constant 114 nm, estimated from figure 4.5, added to the entire pattern in order to make the effective reflectivities at $\phi = 0$ and $\phi = \pi$ equal. These are much more similar to figure 5.6; the most apparent discrepancy is that the spot in the center becomes a problem at high N. This is because of aliasing.

At high N, aliasing in the phase plate becomes a problem. The middle section of the phase plate where aliasing causes 'garbage' necessarily gets larger for smaller slice angles. Figure 5.10 shows the actual $N = 10$ phase plate calculated for the MMA's 200×240 grid, overlaid with the approximate size of the beam spot relative to the MMA. The radius of the garbage is about one-tenth of the beam radius, meaning that approximately 2% of the beam power encounters the garbage.

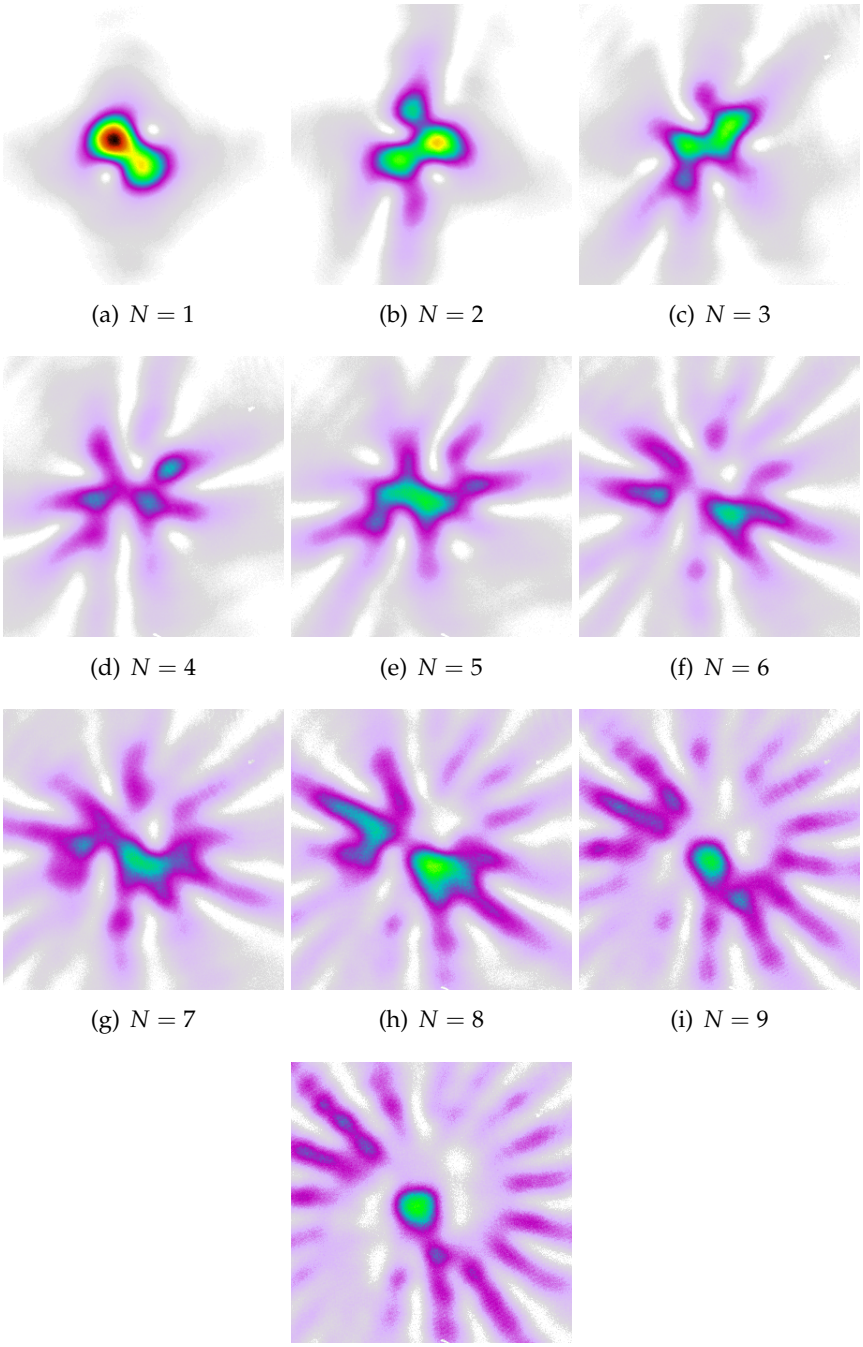

(a) $N = 1$ (b) $N = 2$ (c) $N = 3$

(d) $N = 4$ (e) $N = 5$ (f) $N = 6$

(g) $N = 7$ (h) $N = 8$ (i) $N = 9$

(j) $N = 10$

Figure 5.9: Measured far field intensity distributions of a Gaussian beam having passed a pie phase plate with N slices, where the effective reflectivity of the sectors with phase 0 and π is approximately equal, and less than unity. Compare figure 5.6.

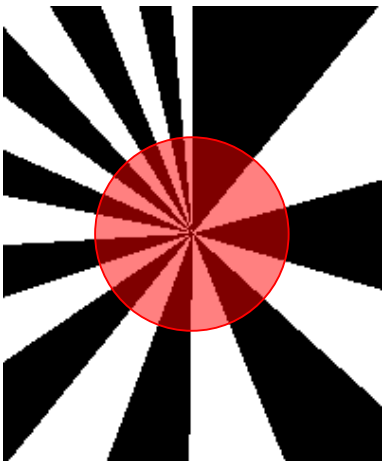

Figure 5.10: Pie phase plate with $N = 10$ slices, rasterized on the MMA's 200×240 grid. White indicates the raised slices with phase difference π. The overlaid red circle is the beam spot, which has a $1/e^2$ intensity radius of 2.05 mm.

6
Conclusion

In this research, we have investigated the suitability of the micro mirror array called *MEMS Phase Former Kit* as a dynamically programmable phase plate for use in orbital angular momentum mode analyzers as described in [13].

The problem of the MMA's limited on-time and required recovery time was solved by the use of software and hardware to synchronize the MMA with the CCD camera. This system can be applied in the same way to any other detector such as a single photon detector, as long as it has some sort of mechanical or software shutter.

A calibration curve for the MMA was determined, relating the address byte of a micro mirror to its actual deflection distance within a margin of error of about 4.5 nm.

The tilting of the mirrors' hinges causes unwanted diffraction effects by spreading intensity from the zero-order to the first and subsequent orders. We have formulated a model which describes these effects in terms of the effective reflectivity of a mirror element as a function of that element's deflection. This problem makes it impossible to accurately reproduce phase patterns with phase gradients, such as spiral phase plates. However, phase patterns with two discrete values 0 and π, such as pie phase plates, can be accurately reproduced, albeit with some loss of intensity.

Aliasing only becomes a concern when attempting to represent structures on the MMA which are thinner than one 'pixel'. This happens near the center of pie phase plates with large numbers of sections.

The MMA's surface curvature causes unwanted and unpredictable distortions in the far field. It may be possible to solve this problem using a phase retrieval algorithm as

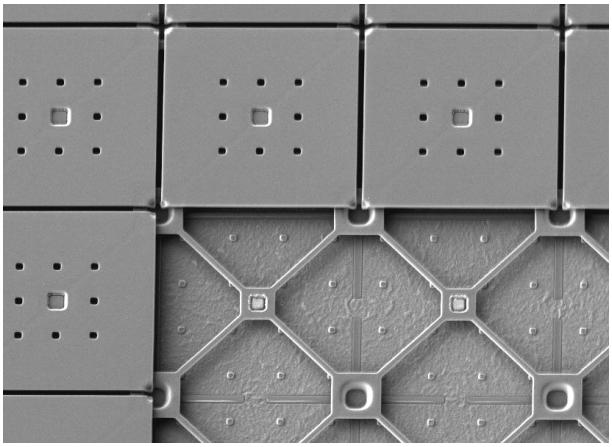

Figure 6.1: SEM photograph of a two-level micro mirror array design (reproduced from [6]).

described in [9]. Another possibility is to use interferometry to map out the surface curvature. Varying the deflection to compensate for the curvature, however, would influence each pixel's effective reflectivity, and it remains to be seen what the effect would be.

In addition, not much is known about the quality of the laser used in these experiments. We recommend using a laser of known quality and phase profile in further experiments.

The Fraunhofer Institute for Photonic Microsystems is still working to improve the design of the *MEMS Phase Former Kit*. A recently published technical report [6] mentioned a two-level mirror design in which the hinges are hidden under the mirrors; figure 6.1 shows an SEM photograph reproduced from that paper. Using a two-level mirror design would eliminate the unwanted diffraction effects caused by the hinges in the current design. As an added advantage, this would also remove one of the obstacles in compensating for the surface curvature, since the mirrors could be deflected by any distance without influencing their effective reflectivity.

Acknowledgements

There is a reason why physics research is done in groups. I would like to acknowledge my supervisors, Bart-Jan Pors and Eric Eliel, for the opportunity to work in the Quantum Optics and Quantum Information group for several enjoyable months; for their patience in the face of bureaucracy; and for sharing ideas for this project that I never could have thought of by myself.

I would also like to acknowledge the Optical Sciences group at the University of Twente, especially my supervisor Martin Jurna. They let me commence my Master's project in April 2007, knowing at the time that I would leave in the middle of it to do this internship, but not knowing that Erik Garbacik would step in to continue the project while I was gone.

Moreover, I am grateful to Wouter Peeters for letting me use his optics equipment; Arno van Amersfoort for manufacturing a custom cable; Daniël Stolwijk for many enoyable discussions in our office, not necessarily about physics; and Gert 't Hooft for taking the time to explain the connection between phase plates and Philips.

A

Some analytical expressions concerning phase plates

A.1 Far field of a Gaussian beam transmitted through a Heaviside phase plate

Consider an input Gaussian beam, in Cartesian coordinates. A Heaviside phase plate (with its phase discontinuity along the y axis in this example) performs its phase operation on the beam, which adds a phase of ϕ to one half of the beam (2.7). We calculate the far field of this system by taking the Fourier transform of the transmitted beam according to (2.2). These functions are separable in x and y:

$$\begin{aligned} E_{\mathrm{FF}}(X,Y) &\propto \mathcal{F}\left\{E_{\mathrm{in}}(x,y)H(x)\right\} \\ &= E_0 \int_{-\infty}^{\infty} e^{-\frac{y^2}{w^2}-i2\pi Yy}dy \left(\int_{-\infty}^{0} e^{-\frac{x^2}{w^2}-i2\pi Xx}dx + e^{-i\phi}\int_{0}^{\infty} e^{-\frac{x^2}{w^2}-i2\pi Xx}dx \right). \end{aligned} \tag{A.1}$$

By way of the following indefinite integral and the properties of the imaginary error function $\operatorname{erfi} z = -i \operatorname{erf} iz$ [11, 01.03.21.0155.01; 06.28.04.0002.01; 06.28.03.0004.01; 06.28.03.0005.01]

$$\int e^{ax^2+bx+c}dx = \frac{\sqrt{\pi}}{2a}e^{c-\frac{b^2}{4a}} \operatorname{erfi}\left(\frac{b+2ax}{2\sqrt{a}}\right); \tag{A.2}$$

$$\operatorname{erfi}(-x) = -\operatorname{erfi}(x); \tag{A.3}$$

$$\operatorname{erfi}(\pm i\infty) = \pm i, \tag{A.4}$$

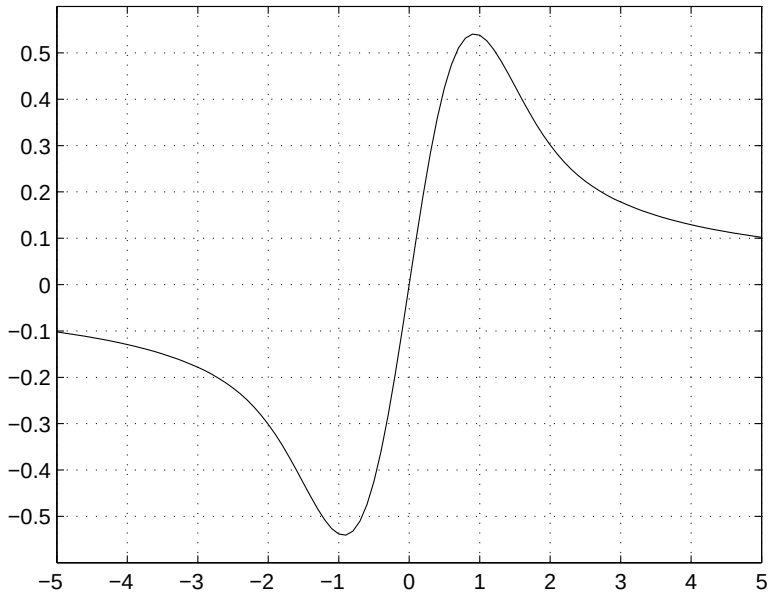

Figure A.1: The Dawson integral $D(x)$.

we obtain

$$E_{\mathrm{FF}}(X,Y) \propto \tfrac{1}{2} i\pi w^2 E_0 e^{-\pi^2 w^2 (X^2+Y^2)} \left((e^{-i\phi}+1)i + (e^{-i\phi}-1)\,\mathrm{erfi}(\pi w X) \right), \tag{A.5}$$

which can be restated in the form of the Dawson integral D, a real-valued function with two extrema on either side of zero, which approaches zero asymptotically as its paramater goes to infinity (figure A.1). It is defined as:

$$D(x) \equiv e^{-x^2} \int_0^x e^{t^2} dt = \tfrac{1}{2}\sqrt{\pi} e^{-x^2}\,\mathrm{erfi}(x). \tag{A.6}$$

This gives us the following general expression for the far field of a Gaussian beam after encountering a Heaviside phase plate:

$$E_{\mathrm{FF}}(X,Y) \propto i\sqrt{\pi} w^2 E_0 e^{-\pi^2 w^2 Y^2} \left((e^{-i\phi}+1)\tfrac{1}{2} i\sqrt{\pi} e^{-\pi^2 w^2 X^2} + (e^{-i\phi}-1) D(\pi w X) \right). \tag{A.7}$$

The intensity is then given by:

$$\begin{aligned} I_{\mathrm{FF}}(X,Y) \propto 2\pi w^4 |E_0|^2 e^{-2\pi^2 w^2 Y^2} \Big(& \frac{\pi}{4}(1+\cos\phi) e^{-2\pi^2 w^2 X^2} \\ & - \sqrt{\pi}\sin\phi\, e^{-\pi^2 w^2 X^2} D(\pi w X) + (1-\cos\phi)(D(\pi w X))^2 \Big). \end{aligned} \tag{A.8}$$

A.2 Far field of a Gaussian beam transmitted through an integer-vorticity spiral phase plate

Since the transmission function of a spiral phase plate (2.12) is more easily expressed in polar coordinates, we will now consider an input Gaussian beam in polar coordinates. Since the transfer function is purely a function of θ and the input field of r, we can again take the Fourier transform of a separable function. Goodman [7, p. something] gives an expression for the Fourier transformation in polar coordinates of a function separable in r and θ:

$$\mathcal{F}\left\{f_r(r)f_\theta(\theta)\right\} = \sum_{k=-\infty}^{\infty} c_k(-i)^k e^{ik\Theta}\mathcal{H}_k\left\{f_r(r)\right\}. \tag{A.9}$$

This is a weighted sum of Hankel transforms, where

$$c_k = \frac{1}{2\pi}\int_0^{2\pi} f_\theta(\theta)e^{-ik\theta}\,d\theta, \tag{A.10}$$

and the Hankel transform is defined as

$$\mathcal{H}_k\left\{f(r)\right\} = 2\pi\int_0^\infty rf(r)J_k(2\pi Rr)\,dr, \tag{A.11}$$

where J_k is the k-th order Bessel function of the first kind. According to Abramowitz and Stegun [1, 11.4.28] the integral's solution is

$$\int_0^\infty e^{-a^2t^2}t^{\mu-1}J_\nu(bt)\,dt = \frac{\Gamma(\frac{1}{2}\nu+\frac{1}{2}\mu)\left(\frac{b}{2a}\right)^\nu}{2a^\mu\Gamma(\nu+1)}\,{}_1F_1\left(\tfrac{1}{2}\nu+\tfrac{1}{2}\mu\,;\,\nu+1\,;\,-\frac{b^2}{4a^2}\right), \tag{A.12}$$

where ${}_1F_1$ is the Kummer confluent hypergeometric function. Using the identity $J_{-k}(z) = (-1)^kJ_k(z)$, formulas [11, 07.20.17.0013.01, 07.20.03.0014.01], and the Legendre duplication formula $\Gamma(z)\Gamma(z+\frac{1}{2}) = 2^{1-2z}\sqrt{\pi}\Gamma(2z)$ [1, 6.1.18], the hypergeometric function can be expanded into two modified Bessel functions of the first kind $I_\alpha(z)$, and we obtain for the Hankel transform of $E_0e^{-r^2/w^2}$:

$$\begin{aligned}&\mathcal{H}_k\left\{E_0e^{-r^2/w^2}\right\} = \\ &\quad(\operatorname{signum}k)^{|k|}\tfrac{1}{2}E_0\pi^{5/2}w^3Re^{-\pi^2w^2R^2/2}\left(I_{(|k|-1)/2}(\tfrac{1}{2}\pi^2w^2R^2) - I_{(|k|+1)/2}(\tfrac{1}{2}\pi^2w^2R^2)\right).\end{aligned} \tag{A.13}$$

For integer vorticity $Q \in \mathbb{Z}$, the coefficients c_k are all zero except for $c_{-Q} = 1$, and we arrive at:

$$\begin{aligned}E_{\mathrm{FF}}(R,\Theta) \propto \tfrac{1}{2}E_0(-i)^{|Q|}e^{-iQ\Theta}\pi^{5/2}w^3Re^{-\pi^2w^2R^2/2}\\ \times\left(I_{(|Q|-1)/2}(\tfrac{1}{2}\pi^2w^2R^2) - I_{(|Q|+1)/2}(\tfrac{1}{2}\pi^2w^2R^2)\right).\end{aligned} \tag{A.14}$$

The intensity is then equal to:

$$I_{\mathrm{FF}}(R) \propto \tfrac{1}{4}|E_0|^2\pi^5 w^6 R^2 e^{-\pi^2 w^2 R^2}\left(I_{(|Q|-1)/2}(\tfrac{1}{2}\pi^2 w^2 R^2) - I_{(|Q|+1)/2}(\tfrac{1}{2}\pi^2 w^2 R^2)\right)^2. \tag{A.15}$$

A.3 Far field of a Gaussian beam transmitted through a pie phase plate

Similar to the spiral phase plate in appendix A.2, the Fourier transform is once again separable into an input field function of r and a transfer function of θ (2.15). We can once again use eqs. (A.9), (A.10), and (A.11), but the coefficients c_k do not vanish in this case. We use this particular Hankel transform's symmetry in k, apparent in (A.13), to express (A.9) as:

$$\mathcal{F}\left\{E_{\mathrm{in}}(r)H(\theta)\right\} = c_0\mathcal{H}_0\left\{E_{\mathrm{in}}(r)\right\} + \sum_{k=1}^{\infty}\left(c_k e^{ik\Theta} + c_k e^{-ik\Theta}\right)(-i)^k\mathcal{H}_k\left\{E_{\mathrm{in}}(r)\right\}. \tag{A.16}$$

We note the special case of the Hankel transform:

$$\mathcal{H}_0\left\{E_0 e^{-r^2/w^2}\right\} = E_0\pi w^2 e^{-\pi^2 w^2 R^2}. \tag{A.17}$$

From (A.10) and the transfer function (2.15) it is straightforward to derive:

$$c_0 = 1 + \frac{1}{\pi}\sum_{p=1}^{2N-1}(-1)^p\alpha_p; \tag{A.18}$$

$$c_k = \frac{i}{\pi k}\sum_{p=0}^{2N-1}(-1)^p e^{ik\alpha_p}; \tag{A.19}$$

$$c_{-k} = \frac{-i}{\pi k}\sum_{p=0}^{2N-1}(-1)^p e^{-ik\alpha_p}. \tag{A.20}$$

We then have

$$\begin{aligned} E_{\mathrm{FF}}(R,\Theta) \propto E_0 w^2 e^{-\pi^2 w^2 R^2}\Bigg(&\pi + \sum_{p=1}^{2N-1}(-1)^p\alpha_p \\ &- \pi^{3/2} wR e^{\pi^2 w^2 R^2/2}\sum_{k=1}^{\infty}\Bigg[\frac{(-i)^k}{k}\left(I_{(|k|-1)/2}(\tfrac{1}{2}\pi^2 w^2 R^2) - I_{(|k|+1)/2}(\tfrac{1}{2}\pi^2 w^2 R^2)\right) \\ &\times \sum_{p=0}^{2N-1}(-1)^p \sin k(\Theta - \alpha_p)\Bigg]\Bigg), \end{aligned} \tag{A.21}$$

and an expression for the intensity $I_{\mathrm{FF}} \propto |E_{\mathrm{FF}}|^2$ is left as an exercise for a computer or a rainy day.

Bibliography

[1] Abramowitz, M., & Stegun, I. A. (Eds.) (1972). *Handbook of mathematical functions with formulas, graphs, and mathematical tables*. National Bureau of Standards, 10th ed.

[2] Aiello, A. (n.d.). Notes.

[3] Allen, L., Beijersbergen, M. W., Spreeuw, R. J. C., & Woerdman, J. P. (1992). Orbital angular momentum of light and the transformation of Laguerre-Gaussian laser modes. *Physical Review A*, *45*(11), 8185–8190.

[4] de Jong, J. A. (2007). *Step-shaped spatial mode converters*. Master's thesis, Universiteit Leiden.

[5] Gehner, A. (2007). MEMS adaptive optics development at IPMS. Presentation. Retrieved 27 November, 2007, from `http://www.ipms.fraunhofer.de/common/SLM_ao_development.pdf`.

[6] Gehner, A., Wildenhain, M., Schmidt, J. U., & Wagner, M. (2007). Recent progress in CMOS integrated MEMS AO mirror development. Tech. rep., Fraunhofer Institute for Photonic Microsystems.

[7] Goodman, J. W. (1996). *Introduction to Fourier optics*. McGraw-Hill, 2nd ed.

[8] Hecht, E. (1998). *Optics*. Addison-Wesley, 3rd ed.

[9] Jesacher, A., Schwaighofer, A., Fürhapter, S., Maurer, C., Bernet, S., & Ritsch-Marte, M. (2007). Wavefront correction of spatial light modulators using an optical vortex image. *Optics Express*, *15*(9), 5801–5808.

[10] Mair, A., Vaziri, A., Weihs, G., & Zeilinger, A. (2001). Entanglement of the orbital angular momentum states of photons. *Nature*, *412*, 313–316.

[11] Marichev, O., & Trott, M. (n.d.). *functions.wolfram.com*. Wolfram Research.

[12] Oemrawsingh, S. S. R. (2004). *Optical dislocations and quantum entanglement*. Ph.D. thesis, Universiteit Leiden.

[13] Pors, J. B., Aiello, A., Oemrawsingh, S. S. R., van Exter, M. P., Eliel, E. R., & Woerdman, J. P. (2008, forthcoming). Angular phase-plate analyzers for measuring the dimensionality of multi-mode fields. In preparation.

[14] Saleh, B. E. A., & Teich, M. C. (1991). *Fundamentals of Photonics*. John Wiley & Sons.

[15] Schmidt, J. U., Knobbe, J., Gehner, A., & Lakner, H. (2007). CMOS integrable micromirrors with highly improved drift-stability. In S. S. Olivier, T. G. Bifano, & J. A. Kubby (Eds.) *Proceedings of the SPIE*, vol. 6467 of *MEMS adaptive optics*, (pp. 64670R 1–11).